Compensation for High-Frequency Vibration of SAR Imaging in the Terahertz Band Based on Linear Chirplet Transform and Empirical Mode Decomposition

Siyu Chen, Yong Wang 🆔, *Senior Member, IEEE*, and Yun Zhang, *Member, IEEE*

Abstract—SAR in THz band is very important and valuable in the field of radar signal processing, and it is much sensitive to the high-frequency vibration of the platform due to the short wavelength. In this article, the high-frequency vibration is characterized as a multicomponent SFM signal, and the parameters estimation method based on the linear chirplet transform and empirical mode decomposition is proposed to compensate for the high-frequency vibration errors. This method can extract the instantaneous frequency of the received signal with high precision, and the focused SAR image can be obtained consequently. Results of simulated and real measured data are provided to illustrate the effectiveness of the novel algorithm proposed in this article.

Index Terms—EMD, high-frequency vibration compensation, LCT, Terahertz synthetic aperture radar (THz-SAR).

NOMENCLATURE

SAR	Synthetic aperture radar.
LCT	Linear chirplet transform.
EMD	Empirical mode decomposition.
IF	Instantaneous frequency.
THz	Terahertz.
SNR	Signal-to-noise ratio.
DSFMT	Discrete sinusoid frequency modulation transform.
PGA	Phase gradient autofocus.
STFT	Short-time Fourier transform.
LFM	Linear frequency modulation.
SFM	Sinusoidal frequency modulation.
APC	Antenna phase center.
RCMC	Range cell migration correlation.
IMF	Intrinsic mode function.
V	Velocity of platform.
H	Height of platform.
$\Delta R_y(t_m)$	High-frequency vibration along the Y-axis.
$\Delta R_z(t_m)$	High-frequency vibration along the Z-axis.
t_m	Slow time.
x_p	X-coordinate of target point P.
y_p	Y-coordinate of target point P.
$R_{Ap}(t_m)$	Slant range between the APC and a target point P.
ΔR	High-frequency vibration error of the platform.
a_i	ith vibration amplitude.
f_i	ith vibration frequency.
φ_i	ith vibration initial phase.
R_p	Shortest slant range between the platform and the target point P.
$\mathrm{rect}(t)$	Window function.
T_r	Chirp pulse duration.
$s(\tau_f, t_m)$	Received signal.
τ_f	Fast time.
σ'_p	Signal amplitude.
c	Velocity of light.
k_r	Frequency modulation rate.
B	Bandwidth.
τ_p	Pulse width.
λ	Transmitted wavelength.
σ_p	Signal amplitude after range compression.
k_a	Doppler frequency modulation rate.
$\omega(t_m)$	Time-varying frequency of $s(t_m)$.
$\omega_{\mathrm{linear}}(t_m)$	Linear component of $\omega(t_m)$.
$\omega_{\sin}(t_m)$	Sinusoidal component of $\omega(t_m)$.
$S(\tau, \omega, \varsigma)$	LCT of $s(t_m)$.
$\mathrm{LCT}[\cdot]$	LCT operator.
τ	LCT time.
ω	LCT frequency.
ς	LCT chirp rate.
$P(t_m)$	LCT kernel.
$h(t_m)$	Window function.
PRF	Pulse repetition frequency.
$\mathrm{res}(t_m)$	Residual signal.
$\mathrm{imf}_i(t_m)$	ith IMF signal.
y_{linear}	Linear signal.
$\mathrm{F}(\alpha_0, \alpha_1)$	Linear fitting objective function.
$\|\|\|_2$	2-norm.

$y_{\sin}$	Sum of sinusoidal signals.
I	Number of sinusoidal signals.
$F(\beta_i, \gamma_i, \delta_i)$	Curve fitting objective function.
H_r	Vibration error compensation function.
H_{ref}	Compensation function for dechirping.

I. INTRODUCTION

SAR is widely used in various fields since its capacity of all-day and all-climate observation [1], [2], [3], [4], [5]. In recent years, terahertz SAR (THz SAR) has attracted more and more attention due to its high imagery resolution and strong antijamming ability. The frequency range of the terahertz wave covers from 0.1 THz to 10 THz, which is between the microwave and infrared rays [6], [7], [8], [9], [10], [11]. THz SAR makes it easier to obtain high-resolution imaging results but it is suffering from the problem of the high-frequency vibration of the platform, which can defocus the imaging results. For the conventional SAR systems, the effect of the high-frequency vibration is almost negligible because its wavelength is much greater than the vibration amplitude. However, for the THz SAR imaging, the tiny vibration of the platform will severely blur the image due to the small wavelength [12]. Since the conventional SAR imaging algorithm cannot compensate for the high-frequency vibration of the platform, it is necessary to study the high-frequency vibration compensation.

In recent years, there are many research works focusing on the compensation of the high-frequency vibration. The wavelet multiresolution analysis in conjunction with the Doppler keystone transform (DKT) and the parametric space projection is presented to estimate the high-frequency vibration [13], [14]. The local fractional Fourier transform (LFrFT) is proposed to estimate and compensate for the high-frequency vibration of the platform [15]. In [16], the adaptive chirplet decomposition is proposed to focus the image for the THz SAR system. The method is effective and easy to be implemented. However, these methods above are only applicable to the single-frequency vibration estimation. In practice, the platform vibration may be very complex, which may include multiple frequencies, so it is necessary to further study the multifrequency vibration estimation.

The fractional Fourier transform (FrFT) with a combination of the quasi-maximum likelihood and the random sample consensus is proposed to compensate for the high-frequency vibration error [17]. The method can estimate the multicomponents vibration error with high estimation accuracy even at a low SNR, but it assumes that the low-frequency motion error has been compensated. In [18] and [19], the vibration estimation method based on the discrete fractional Fourier transform is presented to estimate the instantaneous vibration accelerations and vibration frequencies.

In [20], the DSFMT optimized by the simulated annealing algorithm is used to compensate for the high-frequency vibration of the platform. A method based on the sparsity-promoting parameter estimation is proposed in [21]. This method can reconstruct and compensate for the full aperture phase error upon the single-range bin data. In [22], the method based on the subaperture decomposition and the minimum entropy theorem is used to compensate for the motion error of the THz SAR systems. When there is no isolated strong scatterer in the imaging scene, the method is superior to the PGA algorithm.

The essence of the platform vibration error is the sinusoidal modulation of the phase in the radar return. Therefore, the precondition of the vibration estimation is the analysis of the phase error. At present, some scholars have studied the extraction method of the sinusoidal modulation phase error. In [23] and [24], the time–frequency analysis method based on the STFT is used to obtain the time-frequency representation of the received signals for the estimation of the vibration frequency. But the accuracy of the time–frequency analysis method depends on the length of the short-time window [25]. In addition, the correction method of the phase shift ambiguity is presented in [26] and [27]. This method can extract the sinusoidal modulation phase error when the maximal phase shift between adjacent samples is below π but it does not perform well at low SNR.

To sum up, the main problems of the high-frequency vibration compensation are the multifrequency vibration estimation and the vibration error extraction. To address the limitations of the above method, the LCT in conjunction with the EMD and the curve fitting algorithm is proposed to reconstruct and compensate for the phase error caused by the high-frequency vibration of the platform in this article. After the range compensation, the form of the received signals can be expressed as a hybrid LFM-SFM signal. Therefore, the LCT algorithm is presented to extract the IF of the received signals, which consists of the linear component and the sinusoidal component. Then, the EMD algorithm and the linear fitting algorithm are further used to extract the sinusoidal component, which is introduced by the high-frequency vibration error. Finally, the curve fitting algorithm based on the nonlinear least squares theorem is employed to obtain the parameters of the high-frequency vibration.

The contributions of this article are as follows.

1) The IF extraction method based on the LCT algorithm is employed for the received signals in the THz SAR system, which can accurately extract the IF for the further estimation.

2) Since the received signals after the range compression in the THz SAR system can be expressed as the hybrid LFM-SFM signal, the EMD algorithm and the linear fitting algorithm are used for dechirping the received signals after the range compression to further estimate the vibration parameters.

3) The curve fitting algorithm is applied for the vibration parameter estimation, which can estimate the vibration parameters precisely. Then, after the vibration error compensation using the estimated parameters, the well-focused images can be obtained.

4) Compared with the STFT-based method in [24] and the DSFMT-based method in [20], it can be seen that the proposed algorithm in this article has higher accuracy and computational efficiency.
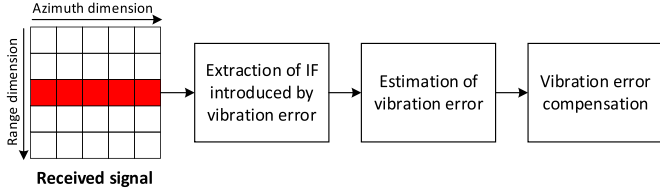
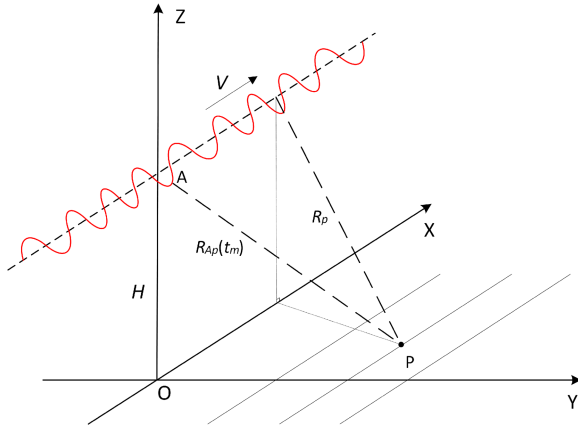Fig. 1. Main work of this article.

Fig. 2. THz SAR imaging geometric model.

The main work of this article is shown in Fig. 1. In the remainder of this work, we first establish the signal model of the radar return with the high-frequency vibration of the platform in Section II. Then, the LCT algorithm in conjunction with the EMD algorithm and the curve fitting algorithm is proposed in Section III. In Section IV, the simulated and real measured data illustrate the effectiveness of the proposed method in this article. Finally, the conclusion to this article is drawn in Section V.

II. IMAGING MODEL OF THz SAR WITH HIGH-FREQUENCY VIBRATION ERROR

The imaging geometric model of the THz SAR is shown in Fig. 2, which works at the vertical side-looking strip mode with the velocity of V and the height H. The dotted line along the X-axis represents the ideal trajectory of the platform, and the red line shows the real trajectory.

Due to the short wavelength of the THz SAR, the high-frequency vibration of the platform cannot be ignored. The platform vibration in practice usually contains multiple frequency components. Since the actual vibration all meet the Dirichlet condition, the high-frequency vibration of the platform can be expressed as the Fourier series [26]. At present, some research works have analyzed the effect of the high-frequency vibration in the SAR imaging. The global positioning system and the inertial measurement unit (IMU) can adjust the pulse repetition frequency according to the platform speed and eliminate the unequal sampling error [27]. Therefore, the vibration error along the azimuth direction has little effect on the final imaging results and only the high-frequency vibration along the Y and Z axes

will be considered [28], which can be expressed as

$$\Delta R_y (t_m) = \sum_{i=1}^{I} a_{yi} \sin (2\pi f_i t_m + \varphi_{yi}) \tag{1}$$

$$\Delta R_z (t_m) = \sum_{i=1}^{I} a_{zi} \sin (2\pi f_i t_m + \varphi_{zi}) \tag{2}$$

where $i = 1, 2, \ldots, I$, t_m represents the slow time. a_{yi} and a_{zi} are the vibration amplitude of the Y and Z axes, respectively, f_i indicates the vibration frequency, φ_{yi} and φ_{zi} denote the initial phase of the platform vibration along the Y and Z axes, respectively.

From Fig. 2, we can see that the real location of the actual APC is $(Vt_m, \Delta R_y, \Delta R_z + H)$. Therefore, the slant range between the APC and a target point P at $(x_p, y_p, 0)$ can be expressed as

$$R_{Ap} (t_m) = \sqrt{(Vt_m - x_p)^2 + (\Delta R_y - y_p)^2 + (\Delta R_z + H)^2}. \tag{3}$$

The amplitude of the high-frequency vibration is usually several millimeters [29], so $\Delta R_y^2 \approx 0$ and $\Delta R_z^2 \approx 0$. After the Taylor expansion, (3) can be rewritten as

$$\Delta R = -\frac{y_p \Delta R_y}{R_p} + \frac{H \Delta R_z}{R_p} = \sum_{i=1}^{I} a_i \sin (2\pi f_i t_m + \varphi_i) \tag{4}$$

$$\begin{aligned} R_{Ap} (t_m) \\ \approx \sqrt{R_p^2 + V^2 t_m^2 - 2y_p \Delta R_y + 2H \Delta R_z + x_p^2 - 2Vt_m x_p} \\ \approx R_p + \Delta R + \frac{V^2 t_m^2}{2R_p} + \frac{x_p^2}{2R_p} - \frac{Vt_m x_p}{R_p} \end{aligned} \tag{5}$$

where ΔR means the high-frequency vibration error of the platform, $R_p = \sqrt{y_p^2 + H^2}$ is the shortest slant range between the platform and the target point $P(x_p, y_p, 0)$. a_i and φ_i are the amplitude and the initial phase of the vibration, respectively.

In THz SAR systems, the chirp signal is commonly used as the transmitting signal. For the target point P, the received signal after demodulation can be expressed as

$$\text{rect} (t) = \begin{cases} 1, & |t| \leq 0.5 T_r \\ 0, & \text{else} \end{cases} \tag{6}$$

$$s (\tau_f, t_m) = \sigma_p' \text{rect} \left(\tau_f - \frac{2R_{Ap} (t_m)}{c} \right)$$

$$\times \exp \left\{ j\pi k_r \left(\tau_f - \frac{2R_{Ap} (t_m)}{c} \right)^2 - j \frac{4\pi}{\lambda} R_{Ap} (t_m) \right\} \tag{7}$$

where $\text{rect}(t)$ denotes the window function, T_r is the chirp pulse duration, τ_f is the fast time, t_m means the slow time, σ_p' represents the signal amplitude, c is the velocity of light, λ denotes the transmitted wavelength. $k_r = \frac{B}{\tau_p}$ means the frequency modulation rate, B is the bandwidth, and τ_p represents the pulse width.

After performing the range compression, the received signal can be expressed as

$$s(\tau_f, t_m) = \sigma_p \sin c \left[\pi B \left(\tau_f - \frac{2R_{Ap}(t_m)}{c} \right) \right]$$
$$\times \exp \left\{ -j\frac{4\pi}{\lambda} R_{Ap}(t_m) \right\} \quad (8)$$

where σ_p is the signal amplitude after the range compression.

Substituting (5) into (8), we can obtain

$$s(\tau_f, t_m) = \sigma_p \sin c \left[\pi B \left(\tau_f - \frac{2R_{Ap}(t_m)}{c} \right) \right]$$
$$\times \exp \left[j \left(\pi k_a t_m^2 + \frac{4\pi V x_p}{\lambda R_p} t_m - \frac{2\pi x_p^2}{\lambda R_p} - \frac{4\pi R_p}{\lambda} - \frac{4\pi \Delta R}{\lambda} \right) \right] \quad (9)$$

where $k_a = -\frac{2V^2}{\lambda R_p}$ indicates the Doppler frequency modulation rate.

After the range cell migration correlation, the received signal can be rewritten as

$$s(\tau_f, t_m) = \sigma_p \sin c \left[\pi B \left(\tau_f - \frac{2R_p}{c} \right) \right]$$
$$\times \exp \left[j \left(\pi k_a t_m^2 + \frac{4\pi V x_p}{\lambda R_p} t_m - \frac{2\pi x_p^2}{\lambda R_p} - \frac{4\pi R_p}{\lambda} \right) \right]$$
$$\times \exp \left[-j\frac{4\pi}{\lambda} \left(\sum_{i=1}^{I} a_i \sin(2\pi f_i t_m + \varphi_i) \right) \right]. \quad (10)$$

From (10), we can see that platform vibration error introduces the sinusoidal modulation phase error in the received signals. Moreover, it is obvious that the amplitude of the phase error is mainly determined by the ratio of the vibration amplitude to the transmitted wavelength. Since the high-frequency vibration amplitude is commonly several millimeters, the wavelength of the conventional SAR is much greater than the vibration amplitude. Therefore, the high-frequency vibration of the platform can be negligible in the conventional SAR systems. However, for the THz SAR systems, its wavelength is equal or even smaller than the high-frequency vibration amplitude. Consequently, the platform vibration error will seriously affect the imaging quality in the THz SAR systems.

In order to compensate for the high-frequency vibration error, the sinusoidal modulation phase error $4\pi \Delta R/\lambda$ needs to be reconstructed first. Therefore, the vibration parameters are estimated by the proposed method in this article; then, the compensation function is constructed. Through the matched filtering, the high-frequency vibration error can be compensated for and the focused images can also be obtained finally.

III. HIGH-FREQUENCY VIBRATION ERROR COMPENSATION METHOD

After the range compression, the received signal is a hybrid LFM-SFM signal. For a range gate, the received signal can be expressed as a hybrid LFM-SFM signal [30], which is shown in (11)

$$s(t_m) = \sigma(t_m) \times \exp\{jp(t_m)\}$$
$$= \sigma(t_m) \times \exp \left[j \left(\pi k_a t_m^2 + \frac{4\pi V x_p}{\lambda R_p} t_m - \frac{2\pi x_p^2}{\lambda R_p} - \frac{4\pi R_p}{\lambda} \right) \right]$$
$$\times \exp \left[-j\frac{4\pi}{\lambda} \left(\sum_{i=1}^{I} a_i \sin(2\pi f_i t_m + \varphi_i) \right) \right]$$
$$= \sigma(t_m) \times \exp \left\{ j \left[A_0 t_m^2 + B_0 t_m - \frac{2\pi x_p^2}{\lambda R_p} - \frac{4\pi R_p}{\lambda} \right] \right\}$$
$$\times \exp \left[j \left(-\frac{4\pi}{\lambda} \sum_{i=1}^{I} a_i \sin(2\pi f_i t_m + \varphi_i) \right) \right] \quad (11)$$

where t_m is the slow time, $\sigma(t_m)$ and $p(t_m)$ are the time-varying amplitude and phase of the signal, respectively. $A_0 = \pi k_a$ means the chirp rate of $s(t_m)$, $B_0 = \frac{4\pi V x_p}{\lambda R_p}$ is the initial frequency of $s(t_m)$, f_i is the modulation frequency, and φ_i means the modulation initial phase.

Therefore, the time-varying frequency $\omega(t)$ of the hybrid LFM-SFM signal can be expressed as

$$\omega(t_m) = \frac{dp(t_m)}{dt_m} = 2A_0 t_m + B_0 - 2\pi$$
$$\times \frac{4\pi}{\lambda} \sum_{i=1}^{I} a_i f_i \cos(2\pi f_i t_m + \varphi_i)$$
$$= \omega_{\text{linear}}(t_m) + \omega_{\sin}(t_m) \quad (12)$$

where $\omega_{\text{linear}}(t_m) = 2A_0 t_m + B_0$ is the linear component of $\omega(t_m)$, $\omega_{\sin}(t_m) = -2\pi \times \frac{4\pi}{\lambda} \sum_{i=1}^{I} a_i f_i \cos(2\pi f_i t_m + \varphi_i)$ is the sinusoidal component of $\omega(t_m)$.

A. IF Reconstruction Based on LCT Algorithm

The LCT algorithm in [31] can represent the energy distribution of the signal in the time–frequency plane. For the time-domain signal $s(t_m)$, the LCT can be defined as

$$S(\tau, \omega, \varsigma) = \text{LCT}[s(t_m)]$$
$$= \int_{-\infty}^{+\infty} s(t_m + \tau) h(t_m) P^*(t_m) dt_m \quad (13)$$

where $\text{LCT}[\cdot]$ means the LCT operator. τ is the time, ω means the frequency, and ς denotes the chirp rate, $P^*(t_m)$ means the complex conjugation of the LCT kernel, $h(t_m)$ is the window function centered at time $t_m = 0$. The integral of the window function over the entire time domain is 1, which can be expressed as

$$\int_{-\infty}^{+\infty} h(t_m) dt_m = 1. \quad (14)$$

The LCT kernel $P(t_m)$ can be defined as

$$P(t_m) = \exp \left[j \left(\omega t_m + \frac{1}{2} \varsigma t_m^2 \right) \right]. \quad (15)$$

In a short period of time $t_m \in [\tau - T/2, \tau + T/2]$, we can consider that the amplitude $\sigma(t_m)$ of the signal is a constant equal to $\sigma(\tau)$. Therefore, (11) can be rewritten as

$$
\begin{aligned}
s(t_m) &= \sigma(\tau) \exp\{jp(t_m)\} \\
&= \sigma(\tau) \exp\left\{j\left[\int \omega(t_m)\,dt_m\right]\right\}.
\end{aligned}
\tag{16}
$$

Then, we perform the Taylor expansion on the frequency $\omega(t_m)$ at time $t_m = \tau$, which can be represented as

$$
\omega(t_m) \approx \omega(\tau) + \varsigma(\tau)(t_m - \tau), t_m \in \left[\tau - \frac{T}{2}, \tau + \frac{T}{2}\right]
\tag{17}
$$

where $\varsigma(\tau) = d\omega(\tau)/\tau$ is the instantaneous chirp rate and T is the window length.

Therefore, the time-varying phase of the signal can be rewritten as

$$
\begin{aligned}
p(t_m) = \omega(\tau)(t_m - \tau) + \frac{\varsigma(\tau)}{2}(t_m - \tau)^2 \\
+ p(\tau), t_m \in \left[\tau - \frac{T}{2}, \tau + \frac{T}{2}\right].
\end{aligned}
\tag{18}
$$

Based on (13), (16), and (18), the LCT of the signal $s(t_m)$ can be represented as

$$
\begin{aligned}
S(\tau, \omega, \varsigma) &= \sigma(\tau) e^{jp(\tau)} \\
&\times \int_{-\infty}^{+\infty} \exp\left\{j\left[(\omega(\tau) - \omega)t_m + \frac{1}{2}(\varsigma(\tau) - \varsigma)t_m^2\right]\right\} \\
&\times h(t_m)\,dt_m.
\end{aligned}
\tag{19}
$$

As shown in (19), when $\omega = \omega(\tau)$, $\varsigma = \varsigma(\tau)$, the LCT of the signal reaches the maximum value in the $\omega-\varsigma$ plane. The domain of ω and ς is $\omega \in [0, 2\pi\text{PRF}/2]$ and $\varsigma \in [-2\pi\text{PRF}/T, 2\pi\text{PRF}/T]$, where PRF is the pulse repetition frequency. According to the Nyquist–Shannon sampling theory, to avoid aliasing, the domain of the frequency ω is $\omega \in [0, 2\pi\text{PRF}/2]$. However, the value of the frequency may be less than 0, so there is a preprocessing process ahead of applying the algorithm. As shown in (20), the time-domain signal $s(t_m)$ is multiplied with $\exp[j(2\pi K t_m)]$, then, the LCT algorithm and the maximum likelihood method are applied to estimate the IF. After that, the final estimation of ω can be obtained by (21)

$$
(\hat{\omega}'(\tau), \hat{\varsigma}'(\tau)) = \underset{\omega, \varsigma}{\arg \max} |\text{LCT}\{s(t_m) \times \exp[j(2\pi K t_m)]\}|
\tag{20}
$$

$$
\hat{\omega}(\tau) = \hat{\omega}'(\tau) - 2\pi K
\tag{21}
$$

where $\hat{\omega}'(\tau)$ and $\hat{\varsigma}'(\tau)$ are the estimation of ω and ς, $\hat{\omega}(\tau)$ is the final estimated result of the frequency. K is a constant, which can usually take the value PRF/4.

It is obvious that the time-varying frequency $\omega(t_m)$ consists of the linear component $\omega_{\text{linear}}(t_m)$ and the sinusoidal component $\omega_{\sin}(t_m)$. Hence, in order to extract the sinusoidal modulation phase error, the EMD algorithm and the linear fitting algorithm

are used to further process the reconstructed frequency $\hat{\omega}(t_m)$, which will be discussed next.

B. Vibration Error Extraction Based on EMD Algorithm and Linear Fitting Algorithm

In 1998, the EMD algorithm is first proposed by Huang et al. [32]. This method can decompose the signals without the basis function, so it has obvious advantages in the signal decomposition, especially in the nonstationary and nonlinear signal decomposition.

The aim of the EMD algorithm is to decompose the signal into a few IMFs. An IMF satisfies the following two conditions.
1) The number of the extreme points and the zero-crossings must be equal or differ by at most one in the entire dataset.
2) At any point, the mean value of the upper envelope defined by the local maxima and the lower envelope defined by the local minima is zero.

For the reconstructed frequency $\hat{\omega}(t_m)$ mentioned above, the EMD algorithm flow is as follows.
1) We first initialize the input signal, just as follows:

$$
x(t_m) = \text{res}(t_m) = \hat{\omega}(t_m)
\tag{22}
$$

where $\text{res}(t_m)$ is the residual signal.
2) The ith IMF can be obtained via circling from 2) to 5). We search for the local extreme point of the input signal to get the upper envelope $y_{\max}$ and the lower envelope $y_{\min}$ of $x(t_m)$ via the cubic splines interpolation.
3) Calculate the mean of the upper and lower envelopes, which can be expressed as

$$
m(t_m) = \frac{1}{2}(y_{\max} + y_{\min}).
\tag{23}
$$

4) The kth sifting result $v_k(t_m)$ can be obtained by (24) $(v_0(t_m) = x(t_m))$

$$
v_k(t_m) = v_{k-1}(t_m) - m(t_m).
\tag{24}
$$

5) In order to ensure the enough physical sense of each IMF, we use the standard deviation SD to stop the circle, which can be set between 0.2 and 0.3. The standard deviation SD can be calculated by the two consecutive sifting results, just as follows:

$$
\text{SD} = \sum_{t=0}^{T}\left[\frac{|v_{k-1}(t_m) - v_k(t_m)|^2}{v_{k-1}^2(t_m)}\right].
\tag{25}
$$

If SD is out of the threshold, $x(t_m) = v_k(t_m)$, $k = k + 1$ and we return to 2) to continue executing the algorithm. If SD satisfies the presetted threshold, the component $v_k(t_m)$ is designated as an IMF $\text{imf}(t_m)$, that is

$$
\text{imf}_i(t_m) = v_k(t_m).
\tag{26}
$$

6) Calculate the residual signal, which is shown in

$$
\text{res}(t_m) = x(t_m) - \text{imf}_i(t_m).
\tag{27}
$$

7) If the residual signal $\text{res}(t_m)$ is monotonic, the EMD algorithm can end and the signal can be finally expressed as

$$\hat{\omega}(t_m) = \sum_{i=1}^{I} \text{imf}_i(t_m) + \text{res}(t_m). \qquad (28)$$

Otherwise, $x(t_m) = \text{res}(t_m)$ and we return to 2) to extract the $(i+1)$th IMF.

From the above, we can know that the EMD algorithm can decompose the reconstructed frequency $\hat{\omega}(t_m)$ into several IMFs, and the monotonic signal is left as the residual signal finally. The IF of the received signals consists mainly of two components, namely the sinusoidal component and the linear component. Since the EMD algorithm can extract all the components that meet the above conditions as IMFs, and the sinusoidal component meets the two conditions of the IMF, the sinusoidal component can be obtained via the IMFs. Then, the information of the linear component can be obtained via the residual signal. Nevertheless, the residual signal is monotonic but not necessarily linear, so the linear fitting algorithm is used to further extract the linear component via the monotonic residual signal $\text{res}(t_m)$. Then, by subtracting the linear component, the sinusoidal component can be obtained for the vibration error compensation. We set a linear signal model as shown in

$$y_{\text{linear}} = \alpha_1 t_m + \alpha_0 \qquad (29)$$

where α_0 and α_1 mean the intercept and the slope of the linear signal model, respectively.

The linear least squares theorem is used to fit the linear signal, and the corresponding objective function can be defined as

$$F(\alpha_0, \alpha_1) = \|\text{res}(t_m) - y_{\text{linear}}\|_2^2 \qquad (30)$$

where $\|\|_2$ means the 2-norm.

By finding the minimum of $F(\alpha_0, \alpha_1)$, we can obtain the optimal solution of (α_0, α_1), that is

$$(\hat{\alpha}_0, \hat{\alpha}_1) = \underset{\alpha_0, \alpha_1}{\arg\min} F(\alpha_0, \alpha_1) \qquad (31)$$

where $\hat{\alpha}_0$ and $\hat{\alpha}_1$ are the estimation of the intercept and the slope, respectively.

Finally, the estimated linear component can be expressed as

$$\hat{\omega}_{\text{linear}}(t_m) = \hat{y}_{\text{linear}} = \hat{\alpha}_1 t_m + \hat{\alpha}_0 \qquad (32)$$

where $\hat{\omega}_{\text{linear}}(t_m)$ is the estimation of the linear component.

Then, the estimation of the sinusoidal component introduced by the high-frequency vibration error can be obtained via

$$\hat{\omega}_{\text{sin}}(t_m) = \hat{\omega}(t_m) - \hat{\omega}_{\text{linear}}(t_m) \qquad (33)$$

Through the sinusoidal component estimation $\hat{\omega}_{\text{sin}}(t_m)$, the high-frequency vibration parameters can be estimated based on the curve fitting algorithm, which will be discussed next.

C. Vibration Error Estimation Based on Curve Fitting Algorithm

In this section, the curve fitting algorithm based on the nonlinear least squares theorem is used to estimate the parameters of the high-frequency vibration error. In order to fit the sinusoidal component $\hat{\omega}_{\text{sin}}(t_m)$, a sinusoidal signal model is established at first, which can be expressed as a sum of sinusoidal signals as shown in

$$y_{\text{sin}} = \sum_{i=1}^{I} \beta_i \sin(2\pi\gamma_i t_m + \delta_i) \qquad (34)$$

where β_i, γ_i, and δ_i are the amplitude, frequency, and initial phase of the ith sinusoidal signal, and I means the number of sinusoidal signals.

It is worth noting that I can be determined by the number of peaks after the Fourier transform. For the THz SAR systems, the sinusoidal signals with larger amplitudes have greater influence on the imaging results. After the Fourier transform, the more peaks we select, the higher the accuracy of parameter estimation will be. However, the vibration error can also be well compensated by selecting only a few dominant peaks with large amplitudes, and the vibration error compensation accuracy will not be greatly improved if we select more peaks with smaller amplitudes. Therefore, we select the dominant peaks with large amplitudes to determine the number I of the sinusoidal signals in this article. Then, the nonlinear least squares theorem is used to fit the sinusoidal curve, and the corresponding objective function can be defined as

$$F(\beta_i, \gamma_i, \delta_i) = \frac{1}{2}\|\hat{\omega}_{\text{sin}}(t_m) - y_{\text{sin}}\|_2^2. \qquad (35)$$

Through the iterative calculation, we find the minimum of the objective function $F(\beta_i, \gamma_i, \delta_i)$ and the parameters $(\beta_i, \gamma_i, \delta_i)$ corresponding to the minimum are the estimated results, that is

$$\left(\hat{\beta}_i, \hat{\gamma}_i, \hat{\delta}_i\right) = \underset{\beta_i, \gamma_i, \delta_i}{\arg\min} F(\beta_i, \gamma_i, \delta_i) \qquad (36)$$

where $\hat{\beta}_i$, $\hat{\gamma}_i$, and $\hat{\delta}_i$ are the estimation of β_i, γ_i, and δ_i, respectively.

Finally, the vibration error compensation function is established to perform the motion compensation, which is shown in

$$H_r = \exp\left[-j\left(\sum_{i=1}^{I} \frac{\hat{\beta}_i}{\hat{\gamma}_i} \sin\left(2\pi\hat{\gamma}_i t_m + \hat{\delta}_i - \frac{\pi}{2}\right)\right)\right]. \qquad (37)$$

The flowchart of the proposed method in this article is shown in Fig. 3.

IV. EXPERIMENTAL RESULTS

A. Results of Simulated Data

In this section, we carry out the simulations based on the point scatters to illustrate the performance of the proposed method. The model of the seven-point scatters is shown in Fig. 4. In addition, the simulation system parameters are shown in Table I. Since the high-frequency vibration in practice may include one or more frequency components, we establish the single-frequency and multifrequency vibration model, respectively, which will be discussed as follows.
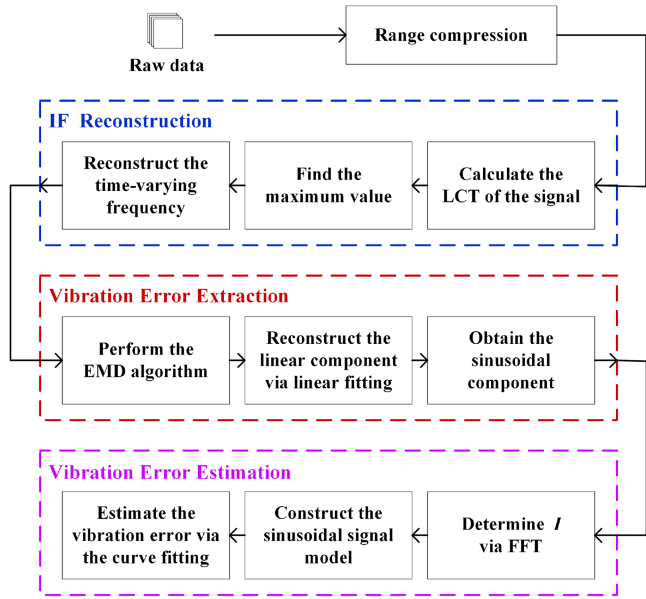
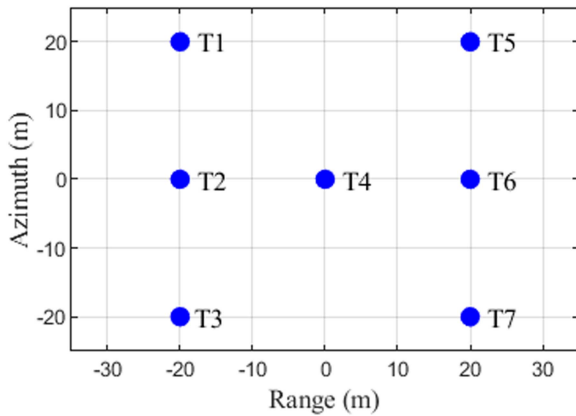Fig. 3. Flowchart of the proposed method in this article.

Fig. 4. Model of the seven-point scatters.

TABLE I
SIMULATION SYSTEM PARAMETERS

Parameters	Values	Parameters	Values
Carrier frequency	220 GHz	Bandwidth	5 GHz
Doppler bandwidth	1760 Hz	SNR	10 dB
Synthetic aperture time	0.5937 s	PRF	2200 Hz
Range resolution	0.03 m	Sampling rate	6 GHz
Azimuth resolution	0.05 m	Pulse width	1 μs
Platform height	3600 m	Platform speed	88 m/s

Case 1: Platform Vibration With Single Frequency

Due to the small wavelength of the THz SAR, the high-frequency vibration error cannot be negligible. Hence, we discuss the platform vibration with the single frequency at first. From (10), we can see that the Doppler rate of the received signals after the range compression is proportional to the square of the platform velocity and inversely proportional to the wavelength and R_p. Due to the large Doppler rate of the received
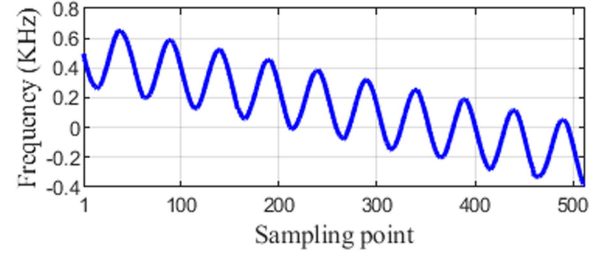
Fig. 5. IF extracted via the LCT algorithm.
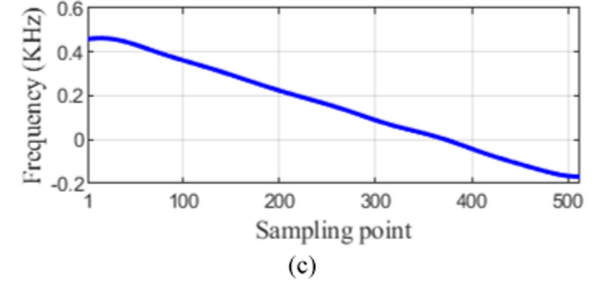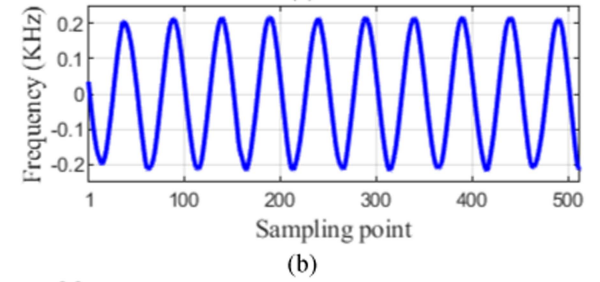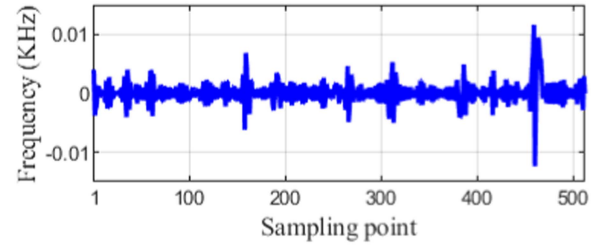
Fig. 6. IMFs and the residual signal extracted via the EMD algorithm. (a) First IMF signal. (b) Second IMF signal. (c) Residual signal.

signals, the range of the IF is also large, which will decrease the accuracy of the LCT-based IF extraction. Therefore, the received signals should be dechirped to narrow the range of the IF at first. After dechirping, the range of the IF is determined by the amplitude of the platform vibration. Since the high-frequency vibration of the platform is usually small, the IF can commonly be extracted precisely via the LCT algorithm after dechirping.

Therefore, we perform the LCT algorithm on a part of the received signal to extract the IF at first. Then, the parameters of the linear component are estimated to construct the compensation function through the EMD algorithm and the linear fitting algorithm. The IF extracted via the LCT algorithm is shown in Fig. 5. The IMFs and the residual signal extracted via the EMD algorithm are shown in Fig. 6, and the linear component fitted via the linear fitting algorithm is shown in Fig. 7.
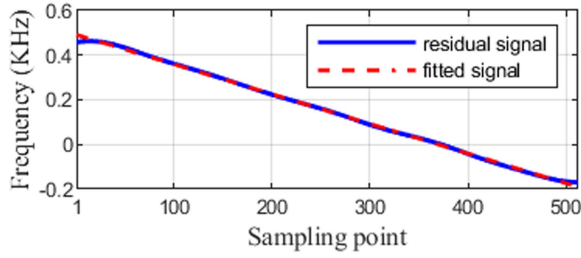
Fig. 7.   Linear component fitted via the linear fitting algorithm.
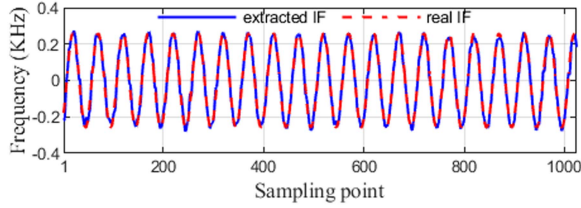

Fig. 8.   IF extracted via the LCT algorithm after dechirping.
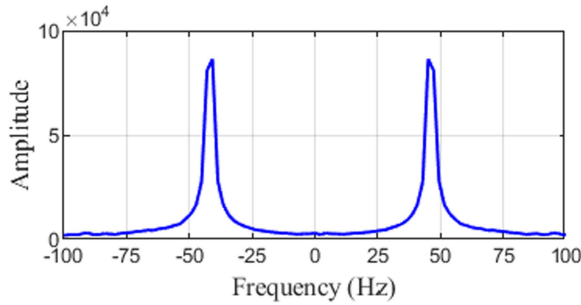

Fig. 9.   Fourier transform result of the IF in Fig. 8.

Then, the compensation function shown in (38) is constructed, and the received signal after range compression is dechirped by multiplying it with

$$H_{\text{ref}} = \exp\left[-j2\pi\left(\frac{\hat{\alpha}_1}{2}t_m^2 + \hat{\alpha}_0 t_m\right)\right] \tag{38}$$

where t_m is the slow time, $\hat{\alpha}_0$ and $\hat{\alpha}_1$ are the intercept and the slope estimation of the residual signal, respectively.

Then, the received signal after dechirping is reused as the input signal $s(t_m)$ in the LCT algorithm to extract its IF, which is shown in Fig. 8. It is obvious that the EMD algorithm and the linear fitting algorithm can dechirp the received signal perfectly, and the LCT algorithm can extract the IF introduced by the vibration error accurately.

Then, the Fourier transform is performed on the extracted IF in Fig. 8 to determine the number I of the extracted sinusoidal signals, which is shown in Fig. 9. It is clear that the number of sinusoidal signals mainly contained in Fig. 8 is 1. Hence, the number I of the extracted sinusoidal signal is 1.

After the Fourier transform, the curve fitting algorithm is used to estimate the vibration error. The estimated vibration parameters are shown in Table II, and the reconstructed IF is

TABLE II
VIBRATION PARAMETERS ESTIMATED VIA THE CURVE FITTING ALGORITHM

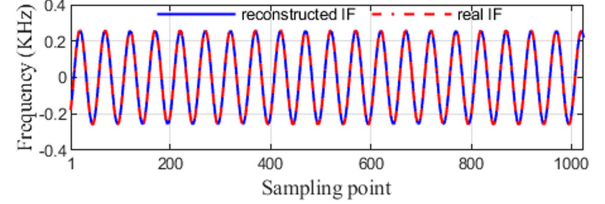| Parameters	Amplitude a_1 (mm)	Frequency f_1 (Hz)	Initial phase φ_1 (rad)
Real values	0.6407	44	0.5585
Estimated values	0.6323	44.0051	0.5513
Absolute error	0.0084	0.0051	0.0072

Fig. 10.   IF reconstructed via the curve fitting algorithm.

shown in Fig. 10. It is worth noting that the vibration parameters shown in Table II are the parameters of ΔR. Nevertheless, the amplitude of the real IF shown in Fig. 10 is calculated by $\frac{4\pi}{\lambda}a_1 f_1$, which is the amplitude of $\omega_{\sin}(t_m)/2\pi$. In addition, the normalized root-mean-square error (NRMSE) defined in the following equation is employed to illustrate the precision of the proposed method

$$\text{NRMSE} = \frac{\|x(t_m) - x_{\text{real}}(t_m)\|_2}{\|x_{\text{real}}(t_m)\|_2} \tag{39}$$

where $x(t_m)$ is the reconstructed IF, and $x_{\text{real}}(t_m)$ denotes the real IF.

The NRMSE of the reconstructed and real phase error is 0.0157. Obviously, the curve fitting algorithm can estimate the vibration parameters precisely, and the phase error can be reconstructed to construct the compensation function defined in (37).

To further illustrate the effectiveness of the proposed method, we used two methods for comparison. The first method is the DSFMT algorithm optimized by the simulated annealing algorithm in [20], and the second method is the STFT algorithm in conjunction with the parameter space projection in [24]. For the second method, instead of using the STFT-based spectrogram for vibration frequency estimation, we extract the time–frequency ridge via the STFT-based spectrogram after dechirping. Then, the Fourier transform is performed on the time–frequency ridge for the vibration frequency estimation, and the parameter space projection is adopted to estimate the vibration amplitude and the vibration initial phase.

The imaging result without the high-frequency vibration compensation is shown in Fig. 11(a), which is defocused in the azimuth dimension. After the vibration error compensation, the imaging results obtained through the STFT-based method in [24] and the DSFMT-based method in [20] are shown in Fig. 11(b) and (c), respectively. The final imaging result obtained through the proposed method is shown in Fig. 11(d). In Fig. 11, the imaging results obtained via different methods are in decibels.

Obviously, the phase error introduced by the platform vibration can be removed via the proposed method in this article
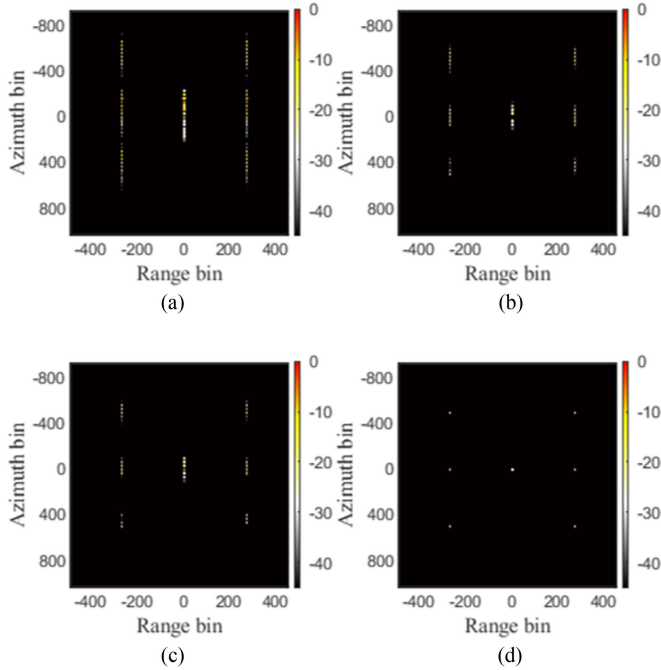
Fig. 11. Imaging results obtained via different methods. (a) Imaging result before the high-frequency vibration compensation. (b) Imaging result after the high-frequency vibration compensation via the STFT-based method in [24]. (c) Imaging result after the high-frequency vibration compensation via the DSFMT-based method in [20]. (d) Imaging result after the high-frequency vibration compensation via the proposed method in this article.
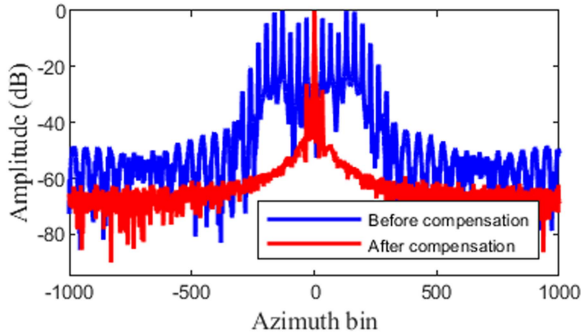

Fig. 12. Azimuth profiles before and after the high-frequency vibration compensation via the proposed method in this article.

and the performance of the proposed method is superior to the STFT-based method in [24] and the DSFMT-based method in [20]. After the vibration error compensation, the azimuth profiles obtained via the proposed method are shown in Fig. 12. It is clear that the well-focused image is obtained and the defocus along the azimuth dimension is suppressed through the proposed method in this article.

Moreover, the image entropy is defined in (40) to further illustrate the performance of the proposed method in this article. The image entropy of Fig. 11 is shown in Table III. Compared with the STFT-based method in [24] and the DSFMT-based method in [20], the proposed method in this article performs better in the high-frequency vibration compensation. In addition, the reduction of the image entropy demonstrates the effectiveness

TABLE III
IMAGE ENTROPY OF FIG. 11

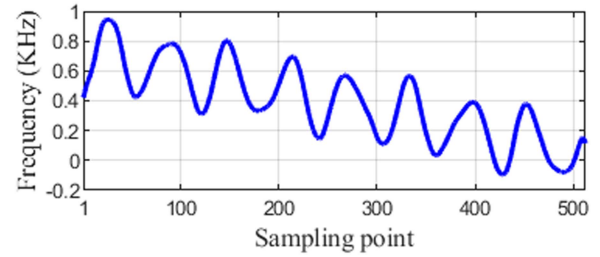| Figs	Fig. 11 (a)	Fig. 11 (b)	Fig. 11 (c)	Fig. 11 (d)
Image entropy	7.6819	6.0670	5.9761	4.5826

Fig. 13. IF extracted via the LCT algorithm.

of the proposed method

$$E = -\sum_{n=1}^{N} \sum_{m=1}^{M} D(n, m) \cdot \ln[D(n, m)] \quad (40)$$

where $D = \frac{|s(n,m)|^2}{E_s}$, $E_s = \sum_{n=1}^{N} \sum_{m=1}^{M} |s(n, m)|^2$, $s(n, m)$ means the discrete image.

Case 2: Platform Vibration With Multiple Frequencies

Then, the high-frequency vibration with multiple frequencies is modeled to further demonstrate the validity of the proposed method. Similarly, we process a part of the received signal at first. The IF obtained via the LCT algorithm is shown in Fig. 13. After the LCT algorithm, the IMFs and the residual signal can be obtained via the EMD algorithm, which is shown in Fig. 14.

The EMD algorithm can be used to distinguish several major sinusoidal signals. However, it may be accidental, that is, the EMD algorithm does not always separate several sinusoidal signals independently. Therefore, the linear fitting algorithm is used to compensate for the linear component to further estimate the vibration parameters.

Then, as shown in Fig. 15, the linear fitting algorithm is employed to fit the residual signal. Through the linear fitting algorithm, the parameters of the linear component are obtained to construct the compensation function defined in (38) for dechirping. Then, the LCT algorithm is reused to extract the IF after dechirping, which is shown in Fig. 16. It is clear that the LCT algorithm can extract the IF with multiple frequencies precisely.

After the IF extraction, the Fourier transform is performed on the extracted IF in Fig. 16 to determine the number I of the extracted sinusoidal signals, which is shown in Fig. 17. Hence, the number I of the extracted sinusoidal signals is 2.

Then, the curve fitting algorithm is used to estimate the parameters of the vibration error, which are shown in Table IV. In addition, the reconstructed IF is shown in Fig. 18. Similarly, the vibration parameters shown in Table IV are the parameters of ΔR, and the amplitudes of the real IF shown in Fig. 18 are calculated by the amplitude of $\omega_{\sin}(t_m)/2\pi$. Moreover, the NRMSE of the reconstructed and real phase error is 0.0206.

TABLE IV
VIBRATION PARAMETERS ESTIMATED VIA THE CURVE FITTING ALGORITHM

Parameters	Amplitude (mm)		Frequency (Hz)		Initial phase (rad)	
	a_1	a_2	f_1	f_2	φ_1	φ_2
Real values	0.7048	0.1281	36	58	0.2094	1.1519
Estimated values	0.6947	0.1227	35.9865	57.9576	0.2080	1.1352
Absolute error	0.0101	0.0054	0.0135	0.0424	0.0014	0.0167
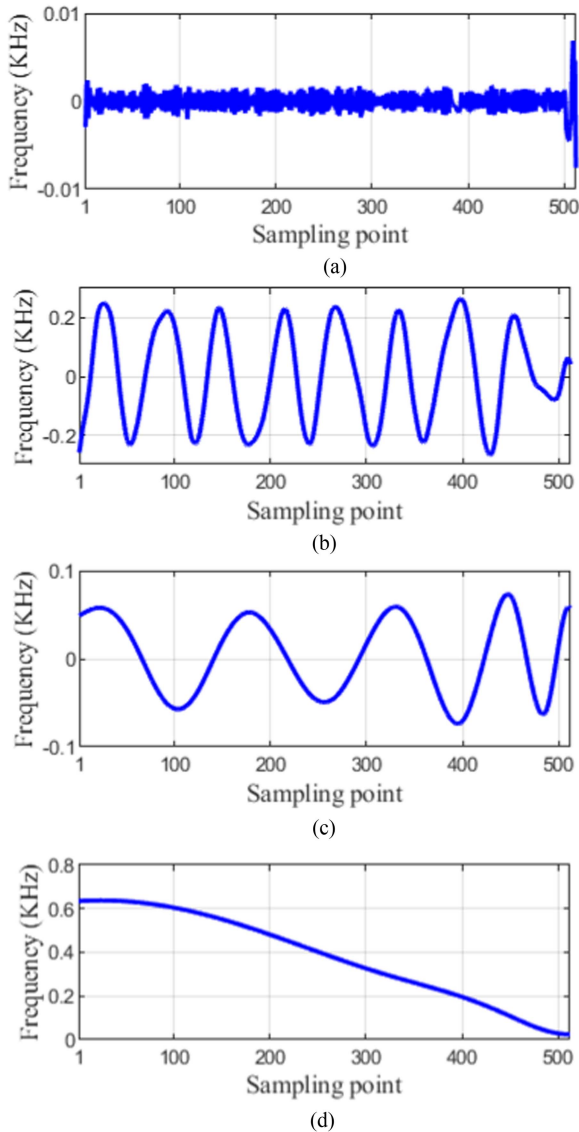
Fig. 14. IMFs and the residual signal extracted via the EMD algorithm. (a) First IMF signal. (b) Second IMF signal. (c) Third IMF signal. (d) Residual signal.
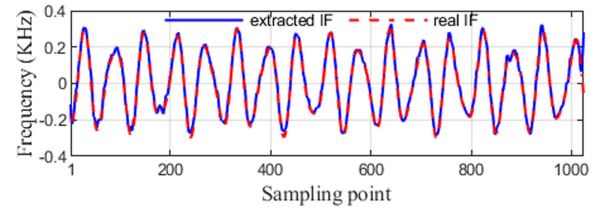

Fig. 15. Linear component fitted via the linear fitting algorithm.

Fig. 16. IF extracted via the LCT algorithm after dechirping.

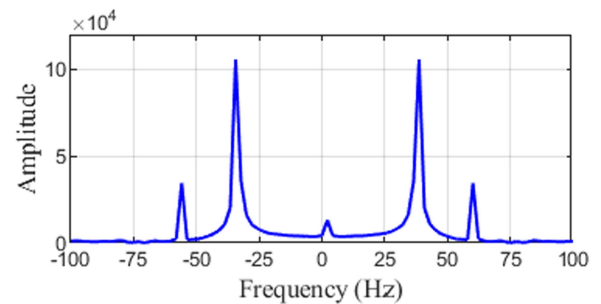Fig. 17. Fourier transform result of the IF in Fig. 16.

It is obvious that the curve fitting algorithm can estimate the vibration error accurately. Through the parameter estimation, the compensation function defined in (37) can be constructed and the sinusoidal modulation phase error can be removed through the matched filtering.

As shown in Fig. 19(a), the imaging result without the high-frequency vibration compensation is defocused in the azimuth dimension. Then, the two methods mentioned above are employed for comparison. The imaging results obtained via the STFT-based method in [24] and the DSFMT-based method in [20] are shown in Fig. 19(b) and (c), respectively. In addition, the proposed method is used to perform the vibration error compensation and the well-focused imaging result is shown in Fig. 19(d). In Fig. 19, the imaging results obtained via different methods are in decibels. Obviously, compared with the STFT-based method in [24] and the DSFMT-based method in [20], the proposed method has higher precision for high-frequency vibration error compensation.

After the high-frequency vibration compensation, the azimuth profiles obtained via the proposed method are shown in Fig. 20, from which we can see that the defocus along the azimuth dimension is depressed via the proposed method in this article.
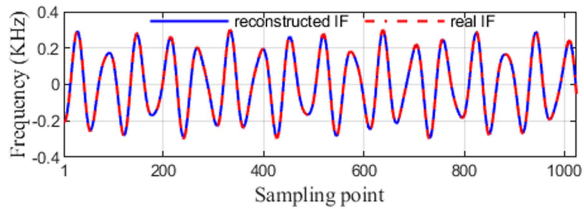
Fig. 18.   IF reconstructed via the curve fitting algorithm.
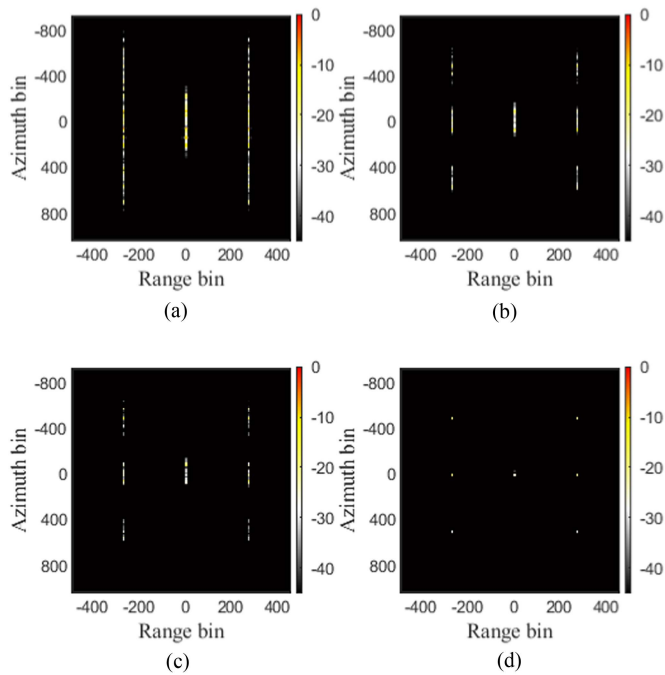

Fig. 19.   Imaging results obtained via different methods. (a) Imaging result before the high-frequency vibration compensation. (b) Imaging result after the high-frequency vibration compensation via the STFT-based method in [24]. (c) Imaging result after the high-frequency vibration compensation via the DSFMT-based method in [20]. (d) Imaging result after the high-frequency vibration compensation via the proposed method in this article.

TABLE V
IMAGE ENTROPY OF FIG. 19

Figs	Fig. 19 (a)	Fig. 19 (b)	Fig. 19 (c)	Fig. 19 (d)
Image entropy	8.6325	7.2756	6.6971	4.6352

Finally, the image entropy of Fig. 19 is used to further illustrate the performance of the proposed method, which is shown in Table V. Compared with the STFT-based method in [24] and the DSFMT-based method in [20], the proposed method has better performance in the vibration error compensation. Apart from that, the decrease in the image entropy demonstrates the superiority of the proposed method in the high-frequency vibration error compensation.

In addition, for the platform vibration with multiple frequencies, we construct 50 Monte Carlo simulations under different SNRs to verify the performance of the proposed algorithm. The average NRMSEs of the reconstructed and real phase error are shown in Table VI. It is clear that the proposed method in this
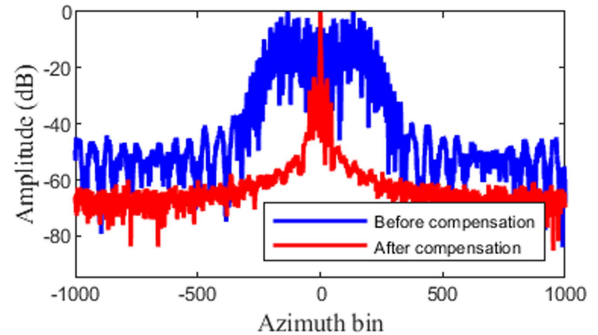

Fig. 20.   Azimuth profiles before and after the high-frequency vibration compensation via the proposed method in this article.

TABLE VI
AVERAGE NRMSEs AND COMPUTATIONAL TIME AT DIFFERENT SNRs

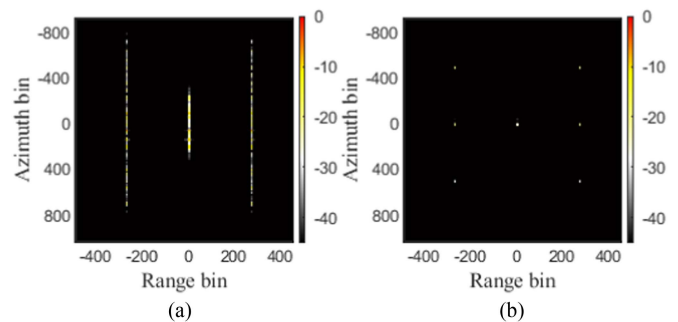| SNR (dB)	NRMSE			Time (s)		
	STFT	DSFMT	LCT	STFT	DSFMT	LCT
0	0.2223	0.1891	0.0398	93.5310	1425.2	1.3623
5	0.2076	0.1881	0.0223	92.2016	1375.0	1.3524
10	0.2189	0.1832	0.0197	96.2909	1432.6	1.3890

Fig. 21.   Imaging results obtained via the proposed method at the SNR of 0 dB. (a) Imaging result before the high-frequency vibration compensation at the SNR of 0 dB. (b) Imaging result after the high-frequency vibration compensation at the SNR of 0 dB.

article has high precision. Moreover, we evaluate the computational efficiency of the proposed algorithm and other algorithms. The specifications of the computer for the simulations are Intel i7-12700 2.11GHz CPU, 32GB RAM. Since the STFT-based method in [24] and the DSFMT-based method in [20] deal with the received signal after dechirping, we list the average computational time at different SNRs after dechirping in Table VI. Obviously, the computational efficiency of the proposed method in this article is higher than that of the STFT-based method in [24] and the DSFMT-based method in [20].

Furthermore, at the SNR of 0 dB, the imaging result before the vibration error compensation is shown in Fig. 21(a). Then, after the vibration error compensation via the proposed method in this article, the well-focused image is shown in Fig. 21(b). The image entropies for Fig. 21(a) and (b) are 12.3035 and 9.6142, respectively. It is obvious that the defocus caused by the vibration error is well eliminated, and the proposed method still performs well even at a low SNR.
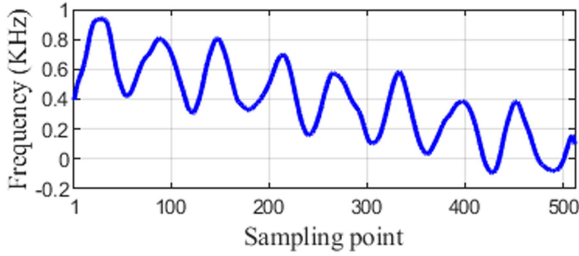
Fig. 22.   IF extracted via the LCT algorithm when the observation targets encounter the perturbation of random motion.
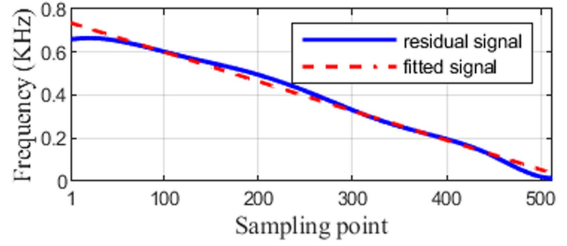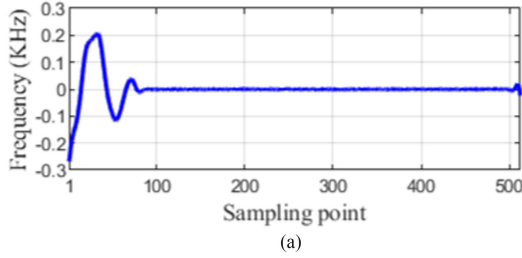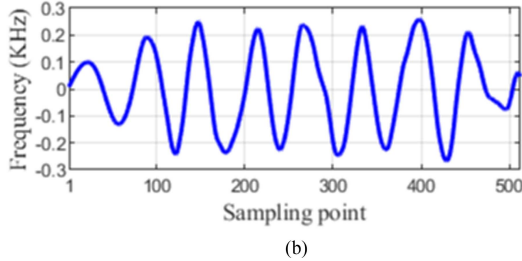

(a)

(b)

(c)

(d)

Fig. 23.   IMFs and the residual signal extracted via the EMD algorithm when the observation targets encounter the perturbation of random motion. (a) First IMF signal. (b) Second IMF signal. (c) Third IMF signal. (d) Residual signal.
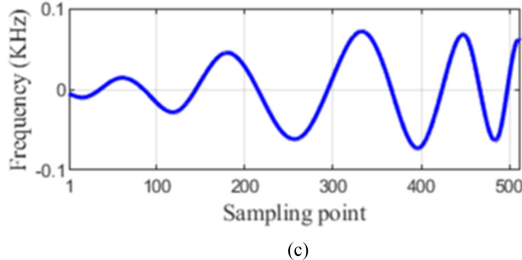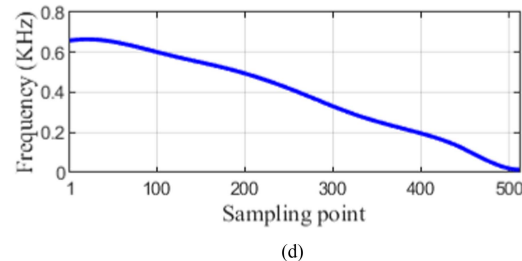
Case 3: Observed Targets With Perturbation of Random Motion

In practice, the observed targets may encounter the perturbation of random motion. Therefore, we add the random motion to T2 and T5 in Fig. 4 to prove the effectiveness of the proposed method in this case. In addition, the settings of other simulation

Fig. 24.   Linear component fitted via the linear fitting algorithm when the observation targets encounter the perturbation of random motion.
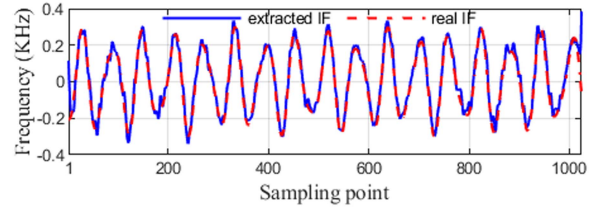

Fig. 25.   IF extracted via the LCT algorithm after dechirping when the observation targets encounter the perturbation of random motion.
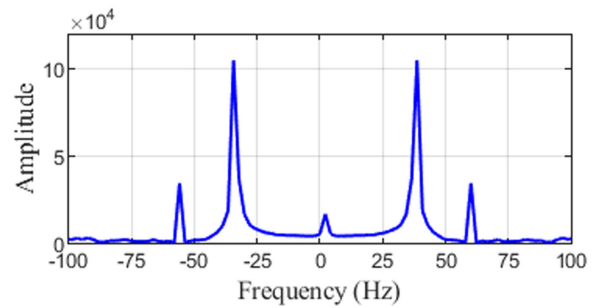

Fig. 26.   Fourier transform result of the IF in Fig. 25 when the observation targets encounter the perturbation of random motion.

experiment parameters in Case 3 are consistent with those of Case 2.

As shown in Fig. 22, the LCT algorithm is performed on a part of the received signal to obtain the IF at first. Then, the EMD algorithm is used to estimate the parameters of the linear component, and the IMFs and the residual signal are shown in Fig. 23.

After the EMD algorithm, the linear fitting algorithm is used to fit the residual signal, which is shown in Fig. 24. Then, the compensation function defined in (38) is employed for dechirping, and the IF after dechirping is extracted via the LCT algorithm, which is shown in Fig. 25. Obviously, the LCT algorithm can still extract the IF when the observed targets encounter the perturbation of random motion.

Then, the Fourier transform is performed on the extracted IF in Fig. 25 to determine the number I of the extracted sinusoidal signals, which is shown in Fig. 26. Obviously, the number of sinusoidal signals mainly contained in Fig. 25 is 2. Therefore, the number I of the extracted sinusoidal signal is 2.

After the Fourier transform, the parameters of the high-frequency vibration are estimated via the curve fitting algorithm,

TABLE VII
VIBRATION PARAMETERS ESTIMATED VIA THE CURVE FITTING ALGORITHM WHEN THE OBSERVATION TARGETS ENCOUNTER THE PERTURBATION OF
RANDOM MOTION

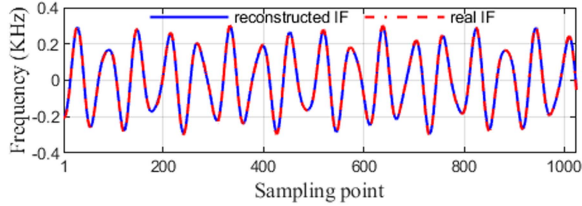| Parameters	Amplitude (mm)		Frequency (Hz)		Initial phase (rad)	
	a_1	a_2	f_1	f_2	φ_1	φ_2
Real values	0.7048	0.1281	36	58	0.2094	1.1519
Estimated values	0.6918	0.1236	35.9751	57.9951	0.1976	1.0918
Absolute error	0.0130	0.0045	0.0249	0.0049	0.0118	0.0601

Fig. 27. IF reconstructed via the curve fitting algorithm when the observation targets encounter the perturbation of random motion.
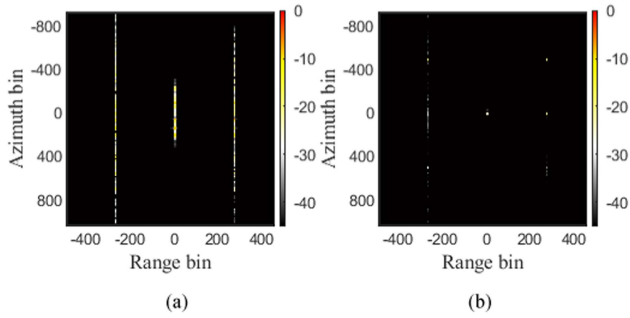

Fig. 28. Imaging results obtained via the proposed method when the observation targets encounter the perturbation of random motion. (a) Imaging result before the high-frequency vibration compensation. (b) Imaging result after the high-frequency vibration compensation.
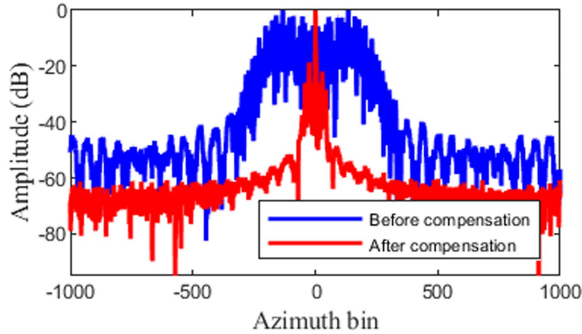

Fig. 29. Azimuth profiles before and after the high-frequency vibration compensation via the proposed method in this article when the observation targets encounter the perturbation of random motion.
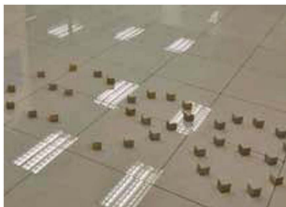

Fig. 30. Actual measured scene.

TABLE VIII
REAL MEASURED SYSTEM PARAMETERS

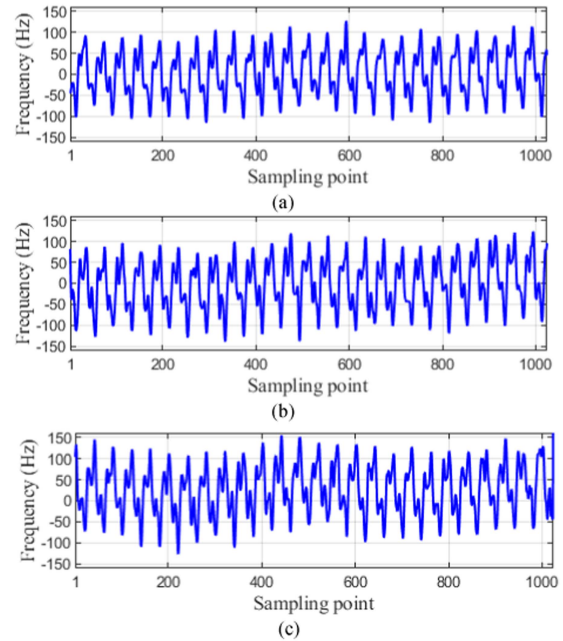| Parameters	Values	Parameters	Values
Center frequency	216 GHz	Bandwidth	4.8 GHz
PRF	2000 Hz	Antenna length	1.2 cm
Range resolution	3.125 cm	Azimuth resolution	3.2 cm
Platform speed	0.35 m/s	Synthetic aperture length	9 cm
Grazing angle	20°	Synthetic aperture time	0.26 s
Platform height	1.2 m	Center slant range	4.1761 m

Fig. 31. IF extracted via the LCT algorithm. (a) IF of the radar return in scene 1 extracted via the LCT algorithm. (b) IF of the radar return in scene 2 extracted via the LCT algorithm. (c) IF of the radar return in scene 3 extracted via the LCT algorithm.

which are shown in Table VII. Moreover, the reconstructed IF is shown in Fig. 27, and the NRMSE of the reconstructed and real phase error is 0.0310. Then, the compensation function defined in (37) is constructed for the high-frequency vibration compensation.

The imaging results before and after the high-frequency vibration compensation via the proposed method in this article are shown in Fig. 28(a) and (b), respectively. Moreover, the image entropies for Fig. 28(a) and (b) are 9.0320 and 5.7631, respectively. As shown in (b), the point targets without the random motion are clearly visible, and the defocus along the azimuth dimension that still exists after the vibration compensation is
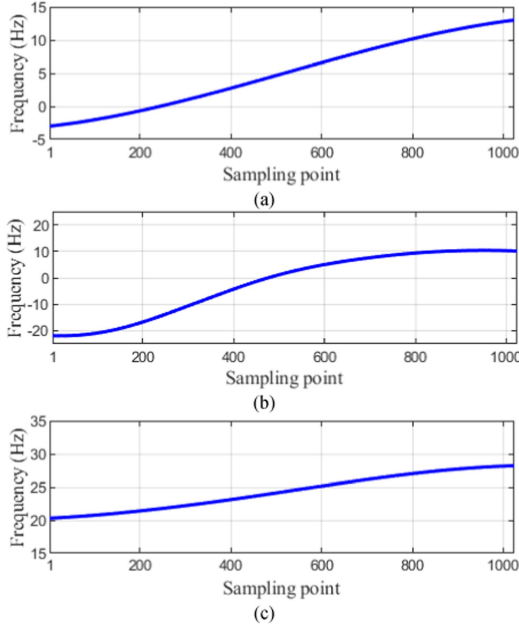
Fig. 32. Residual signals obtained by the EMD algorithm. (a) Residual signal obtained by the EMD algorithm in scene 1. (b) Residual signal obtained by the EMD algorithm in scene 2. (c) Residual signal obtained by the EMD algorithm in scene 3.
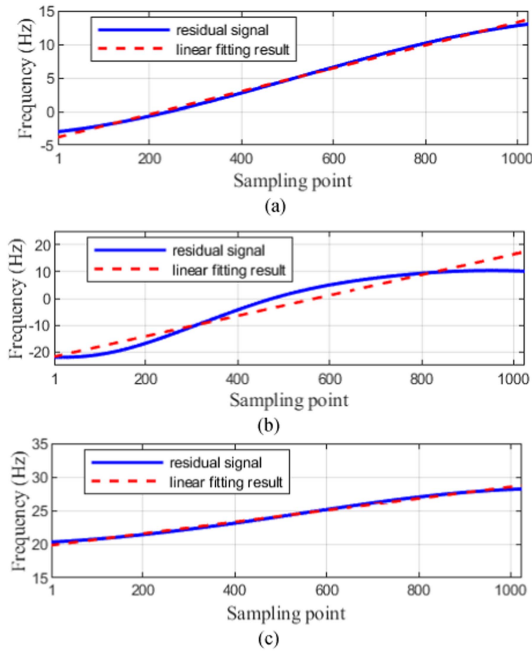

Fig. 33. Linear components fitted by the linear fitting algorithm. (a) Linear component fitted by the linear fitting algorithm in scene 1. (b) Linear component fitted by the linear fitting algorithm in scene 2. (c) Linear component fitted by the linear fitting algorithm in scene 3.

caused by the random motion of the point targets. Moreover, the azimuth profiles obtained via the proposed method are shown in Fig. 29. Therefore, when the observed targets encounter the perturbation of random motion, the proposed algorithm can still compensate for the high-frequency vibration error of the platform well.
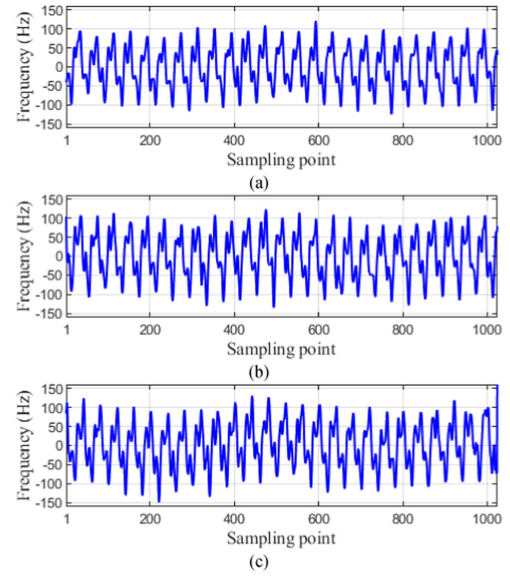
Fig. 34. Sinusoidal components introduced by the high-frequency vibration error. (a) Sinusoidal component introduced by the high-frequency vibration error in scene 1. (b) Sinusoidal component introduced by the high-frequency vibration error in scene 2. (c) Sinusoidal component introduced by the high-frequency vibration error in scene 3.
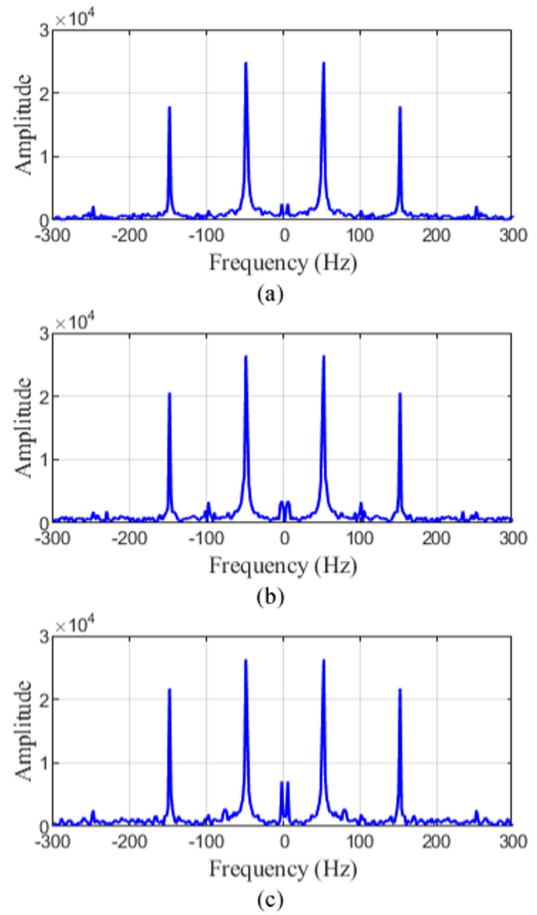

Fig. 35. Fourier transform results of the sinusoidal components in Fig. 34. (a) Fourier transform result of the sinusoidal component in Fig. 34(a). (b) Fourier transform result of the sinusoidal component in Fig. 34(b). (c) Fourier transform result of the sinusoidal component in Fig. 34(c).
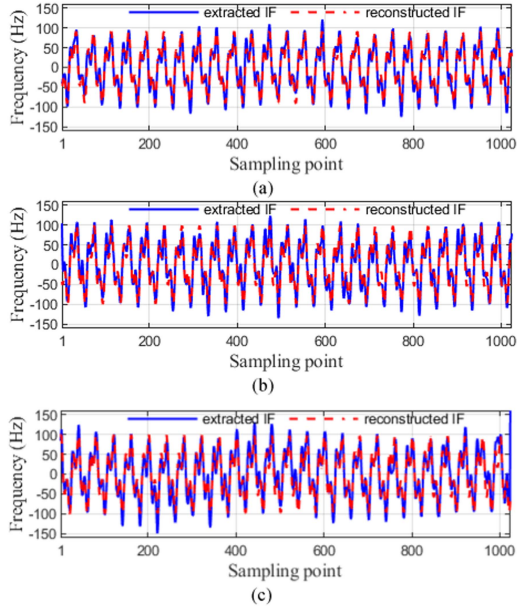
Fig. 36. IFs reconstructed via the curve fitting algorithm. (a) IF reconstructed via the curve fitting algorithm in scene 1. (b) IF reconstructed via the curve fitting algorithm in scene 2. (c) IF reconstructed via the curve fitting algorithm in scene 3.

TABLE IX
IMAGE ENTROPY OF FIG. 37

Scene 1 (digit **8**)	Image entropy	Scene 2 (digit **6**)	Image entropy	Scene 3 (digit **3**)	Image entropy
Fig. 37 (a)	9.5888	Fig. 37 (e)	9.9220	Fig. 37 (i)	9.9214
Fig. 37 (b)	9.5770	Fig. 37 (f)	9.8978	Fig. 37 (j)	9.8799
Fig. 37 (c)	8.4126	Fig. 37 (g)	9.8519	Fig. 37 (k)	8.9054
Fig. 37 (d)	8.3919	Fig. 37 (h)	8.8398	Fig. 37 (l)	8.8223

B. Results of Real Measured Data

In this section, the real measured data are used to validate the proposed method in this article. The actual measured scene shown in Fig. 30 is composed of corner reflectors, and the system parameters are shown in Table VIII. The radar is placed on the trolley, which works at the vertical side-looking mode, and the vertical range from the scene to the radar is 4 m. Moreover, the measurement is in the chamber.

Due to the different response of the frequency source and other components in the signal bandwidth, the amplitude-phase errors are introduced into the received signals, which will severely affect the system performance. Therefore, the compensation method in [33] is used to compensate for the systematic amplitude-phase errors at first.

In this article, we process the three scenes "8," "6," and "3," respectively. Since the Doppler rate of the real measured data is small, the complete IF can be extracted via (20) and (21) directly. After the extraction of the IF, the EMD algorithm and the linear fitting algorithm are used to estimate and reconstruct the linear component of the IF. By subtracting the linear component, the sinusoidal component of the IF introduced via the high-frequency vibration error can be reconstructed.
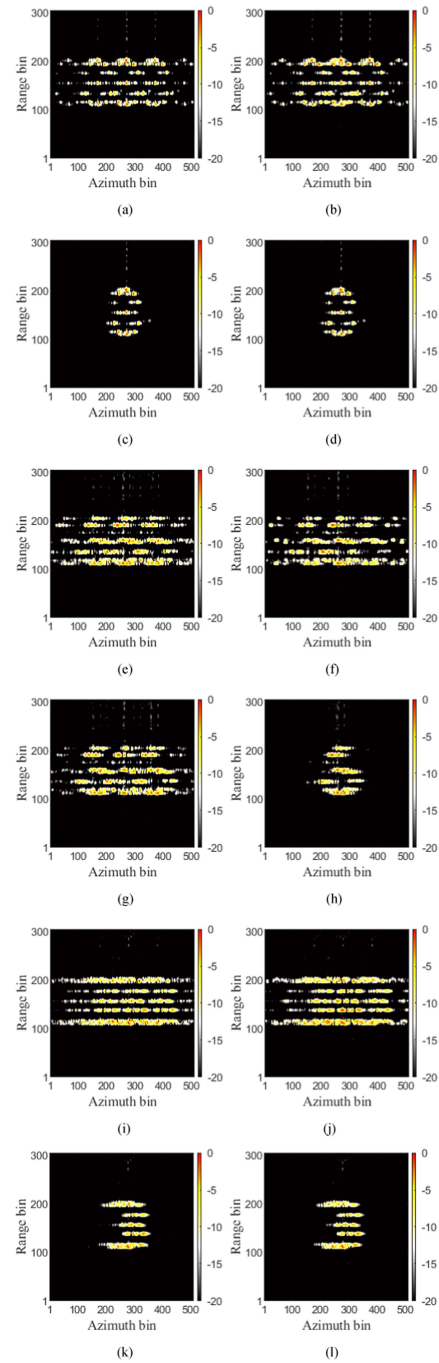

Fig. 37. Imaging results obtained via different methods. (a) Imaging result of scene 1 before the high-frequency vibration compensation. (b) Imaging result of scene 1 after the high-frequency vibration compensation via the STFT-based method in [24]. (c) Imaging result of scene 1 after the high-frequency vibration compensation via the DSFMT-based method in [20]. (d) Imaging result of scene 1 after the high-frequency vibration compensation via the proposed method in this article. (e) Imaging result of scene 2 before the high-frequency vibration compensation. (f) Imaging result of scene 2 after the high-frequency vibration compensation via the STFT-based method in [24]. (g) Imaging result of scene 2 after the high-frequency vibration compensation via the DSFMT-based method in [20]. (h) Imaging result of scene 2 after the high-frequency vibration compensation via the proposed method in this article. (i) Imaging result of scene 3 before the high-frequency vibration compensation. (j) Imaging result of scene 3 after the high-frequency vibration compensation via the STFT-based method in [24]. (k) Imaging result of scene 3 after the high-frequency vibration compensation via the DSFMT-based method in [20]. (l) Imaging result of scene 3 after the high-frequency vibration compensation via the proposed method in this article.
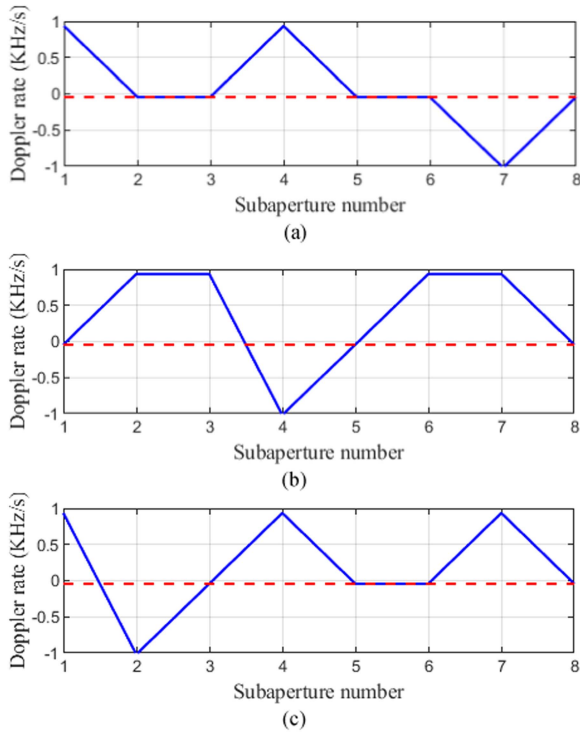
Fig. 38. Doppler rate estimation after the high-frequency vibration compensation. (a) Doppler rate estimation after the high-frequency vibration compensation in scene 1. (b) Doppler rate estimation after the high-frequency vibration compensation in scene 2. (c) Doppler rate estimation after the high-frequency vibration compensation in scene 3.

After the compensation of the amplitude-phase errors, the proposed method is employed for the compensation of the high-frequency vibration error. As shown in Fig. 31, the IFs of the radar return in the three scenes are extracted via the LCT algorithm, which include the linear components and the sinusoidal components.

Then, the EMD algorithm is performed on the IFs, and the residual signals obtained by the EMD algorithm are shown in Fig. 32. After the EMD algorithm, the linear components fitted by the linear fitting algorithm are shown in Fig. 33. After estimating the linear components of the IFs via the linear fitting algorithm, the sinusoidal components introduced by the high-frequency vibration error can be obtained via subtracting the linear components from the IFs.

As shown in Fig. 34, the sinusoidal components introduced by the high-frequency vibration error are obtained by subtracting the estimated linear components from the IFs. It is obvious that the sinusoidal components are periodic and include multiple frequency components. Hence, the multicomponent sinusoidal model is further used for the reconstruction of the vibration error.

As shown in Fig. 35, the Fourier transform is performed on the sinusoidal components in Fig. 34 to determine the number I of the extracted sinusoidal signals. Hence, for the real measured data, we mainly select 2 sinusoidal signals for the vibration error compensation.

Then, the curve fitting algorithm is performed to estimate the parameters of the vibration error, and the reconstructed IFs are

TABLE X
IMAGE ENTROPY OF FIG. 40

Scene 1 (digit **8**)	Image entropy	Scene 2 (digit **6**)	Image entropy	Scene 3 (digit **3**)	Image entropy
Fig. 40 (a)	9.8769	Fig. 40 (d)	9.3510	Fig. 40 (g)	9.6132
Fig. 40 (b)	8.7350	Fig. 40 (e)	8.2103	Fig. 40 (h)	8.4148
Fig. 40 (c)	7.4631	Fig. 40 (f)	7.3963	Fig. 40 (i)	7.1811

shown in Fig. 36. After the parameter estimation of the vibration error, the compensation function defined in (37) is constructed to compensate for the high-frequency vibration error.

The imaging results of the real measured data without the high-frequency vibration compensation are shown in Fig. 37(a), (e), and (i), respectively. Similarly, the two methods mentioned above are used for comparison in this section. The imaging results obtained via the STFT-based method in [24] are shown in Fig. 37(b), (f), and (j), respectively. In addition, the imaging results obtained via the DSFMT-based method in [20] are shown in Fig. 37(c), (g), and (k), respectively. After the high-frequency vibration compensation via the proposed method in this article, the imaging results are shown in Fig. 37(d), (h), and (l), respectively. In Fig. 37, the imaging results are all in decibels. It is obvious that the defocus along the azimuth dimension is depressed via the proposed method in this article. Compared with the STFT-based method in [24] and the DSFMT-based method in [20], the proposed method has higher precision.

In addition, the image entropy shown in Table IX is used to further illustrate the performance of the proposed method in this article. As shown in the image entropy of scene 1, the first line shows the image entropy before the high-frequency vibration compensation, the second and third lines show the image entropy after the STFT-based method in [24] and the DSFMT-based method in [20], respectively. Furthermore, the last line shows the image entropy after the proposed method in this article, which is the smallest. Compared with the STFT-based method in [24] and the DSFMT-based method in [20], the proposed method in this article performs better in the high-frequency vibration compensation.

Since a large estimation range will increase the computational burden, the STFT-based method in [24] and the DSFMT-based method in [20] need to estimate the approximate range of vibration parameters in advance, and set a small and accurate parameter estimation range. The advantage of the proposed method in this article is that it can directly estimate the vibration parameters without setting the parameter estimation range, and it has high estimation accuracy and fast calculation speed. Furthermore, the STFT-based method in [24] and the DSFMT-based method in [20] estimate the vibration parameters via processing the received signals and finding the extreme value, which cannot obtain high estimation accuracy due to the influence of the noise and the amplitude of the received signals. For the proposed method in this article, the IF introduced by the high-frequency vibration is extracted at first, then the vibration parameter estimation is performed. Therefore, it has higher precision.

Moreover, if the platform is not moving at a constant speed or the platform movement track deviates from the ideal track, the
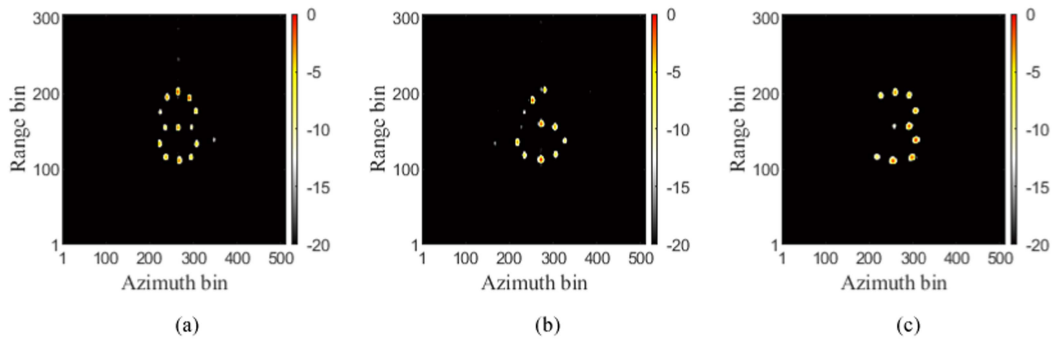
Fig. 39. Imaging results after the high-frequency vibration compensation via the proposed method in this article and the PGA algorithm. (a) Final imaging result of scene 1 after the high-frequency vibration compensation via the proposed method in this article and the PGA algorithm. (b) Final imaging result of scene 2 after the high-frequency vibration compensation via the proposed method in this article and the PGA algorithm. (c) Final imaging result of scene 3 after the high-frequency vibration compensation via the proposed method in this article and the PGA algorithm.

Fig. 40. Imaging results of the first set of data segments. (a) Imaging result of scene 1 before the high-frequency vibration compensation via the proposed method in this article. (b) Imaging result of scene 1 after the high-frequency vibration compensation via the proposed method in this article. (c) Final imaging result of scene 1 after the high-frequency vibration compensation via the proposed method in this article and the PGA algorithm. (d) Imaging result of scene 2 before the high-frequency vibration compensation via the proposed method in this article. (e) Imaging result of scene 2 after the high-frequency vibration compensation via the proposed method in this article. (f) Final imaging result of scene 2 after the high-frequency vibration compensation via the proposed method in this article and the PGA algorithm. (g) Imaging result of scene 3 before the high-frequency vibration compensation via the proposed method in this article. (h) Imaging result of scene 3 after the high-frequency vibration compensation via the proposed method in this article. (i) Final imaging result of scene 3 after the high-frequency vibration compensation via the proposed method in this article and the PGA algorithm.
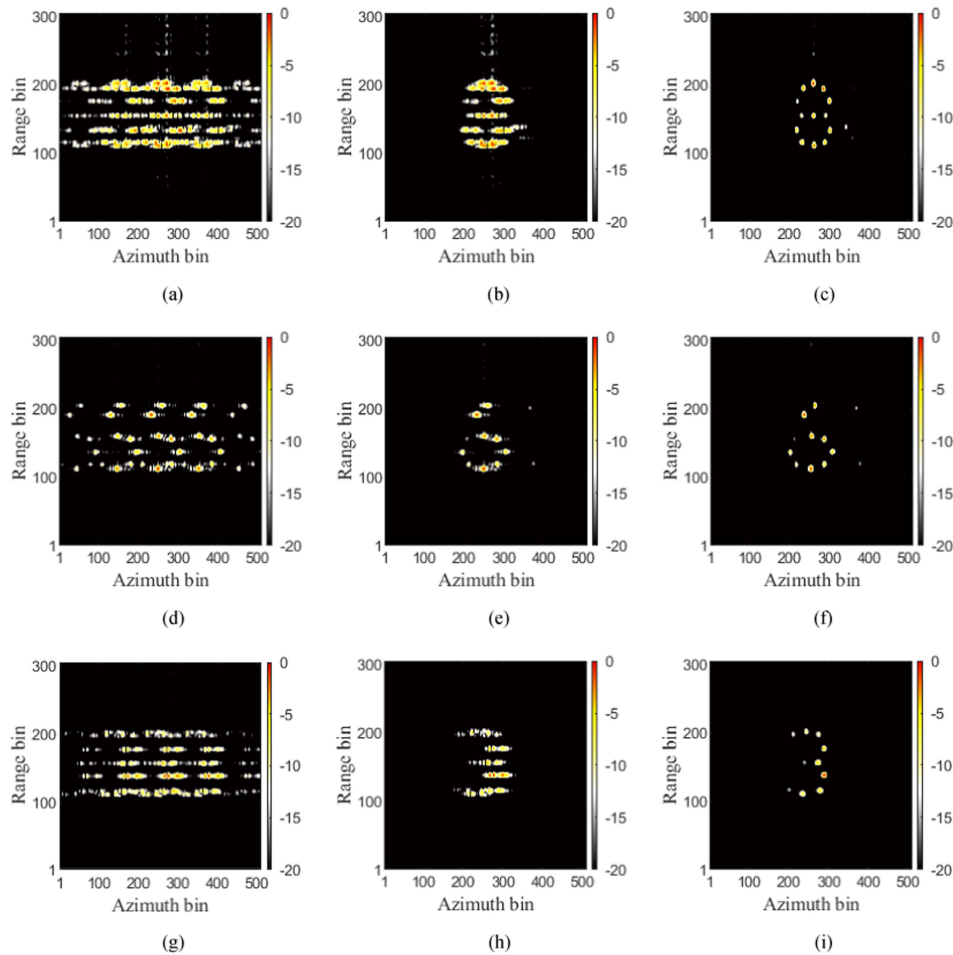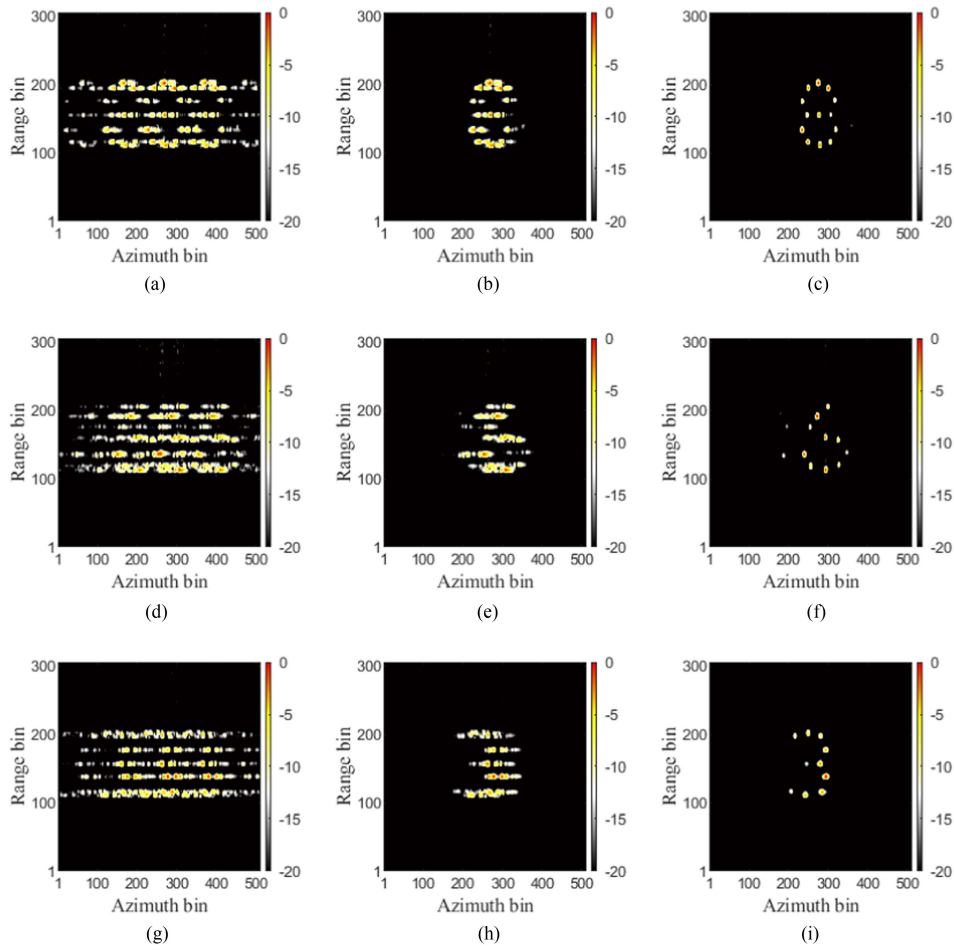
Fig. 41. Imaging results of the second set of data segments. (a) Imaging result of scene 1 before the high-frequency vibration compensation via the proposed method in this article. (b) Imaging result of scene 1 after the high-frequency vibration compensation via the proposed method in this article. (c) Final imaging result of scene 1 after the high-frequency vibration compensation via the proposed method in this article and the PGA algorithm. (d) Imaging result of scene 2 before the high-frequency vibration compensation via the proposed method in this article. (e) Imaging result of scene 2 after the high-frequency vibration compensation via the proposed method in this article. (f) Final imaging result of scene 2 after the high-frequency vibration compensation via the proposed method in this article and the PGA algorithm. (g) Imaging result of scene 3 before the high-frequency vibration compensation via the proposed method in this article. (h) Imaging result of scene 3 after the high-frequency vibration compensation via the proposed method in this article. (i) Final imaging result of scene 3 after the high-frequency vibration compensation via the proposed method in this article and the PGA algorithm.

phase error induced by the velocity variation will occur, which will blur the imaging results. As shown in Fig. 38, the received signals after the high-frequency vibration compensation are divided into eight subaperture signals along the azimuth dimension for the estimation of the Doppler rate. The solid lines show the Doppler rate estimation, and the red dotted lines represent the Doppler rate for the ideal motion of the platform. Therefore, due to the velocity variation of the platform, the imaging results in Fig. 37 are still defocused, which will be further compensated via the PGA algorithm.

After the high-frequency vibration compensation via the proposed method in this article and the PGA algorithm, the well-focused imaging results in decibels are shown in Fig. 39. The image entropies for Fig. 39(a)–(c) are 7.3191, 7.3503, and 7.3511, respectively. Obviously, by using the sinusoidal model with two dominant components to reconstruct the vibration error, the platform vibration error can be compensated and the well-focused images can be obtained. In addition, the defocus along the azimuth dimension is depressed completely, and the images of the three scenes are clearly visible after the proposed method in this article and the PGA algorithm.

For the three scenes in the real measured data, we selected two additional sets of different data segments to further illustrate the effectiveness of the proposed method, respectively. For the first set of data segments, the imaging results of the three scenes are shown in Fig. 40, respectively. The original imaging results without any compensation are shown in Fig. 40(a), (d), and (g), respectively. As shown in Fig. 40(b), (e), and (h), the high-frequency vibration error is compensated via the proposed method in this article, and the defocus along the azimuth dimension is significantly depressed. Finally, the well-focused images are obtained via the PGA algorithm, and the digits are clearly visible, which are shown in Fig. 40(c), (f), and (i), respectively. Moreover, the decrease in the image entropy proves the validity of the proposed method in this article, which is shown in Table X.

TABLE XI
IMAGE ENTROPY OF FIG. 41

Scene 1 (digit **8**)	Image entropy	Scene 2 (digit **6**)	Image entropy	Scene 3 (digit **3**)	Image entropy
Fig. 41 (a)	9.6107	Fig. 41 (d)	9.9264	Fig. 41 (g)	9.7179
Fig. 41 (b)	8.4039	Fig. 41 (e)	8.8190	Fig. 41 (h)	8.5711
Fig. 41 (c)	7.2025	Fig. 41 (f)	7.2141	Fig. 41 (i)	7.3033

Similarly, for the second set of data segments, the imaging results of the three scenes are shown in Fig. 41, respectively. The imaging results before the high-frequency vibration compensation are shown in Fig. 41(a), (d), and (g), respectively. After the high-frequency vibration compensation via the proposed method in this article, the defocus along the azimuth dimension is significantly depressed, which are shown in Fig. 41(b), (e), and (h), respectively. As shown in Fig. 41(c), (f), and (i), the PGA algorithm is employed to obtain the well-focused image, and the digits are clearly visible. In addition, the image entropy is shown in Table XI to further demonstrate the improvement of the image quality.

V. CONCLUSION

In this article, the LCT algorithm in conjunction with the EMD algorithm and the curve fitting algorithm is proposed to compensate for the high-frequency vibration error of the platform. Due to the small wavelength of the THz SAR, the high-frequency vibration of the platform is considerable. Hence, the study for the high-frequency vibration compensation is necessary. The proposed method in this article can estimate and reconstruct the phase error introduced by the high-frequency vibration of the platform. Through the construction of the vibration error compensation function, the vibration error can be compensated and the well-focused imaging results can be achieved. Compared with the STFT-based method in [24] and the DSFMT-based method in [20], the proposed method in this article has better performance. Results of simulated and the real measured data demonstrate the effectiveness and the precision of the proposed method in this article.

Furthermore, the range of the LCT-based IF extraction is limited by the pulse repetition frequency. Since the amplitude of the high-frequency vibration error is usually small, the LCT algorithm can generally extract the IF well. However, if the amplitude of vibration error is too large, the accuracy of LCT-based IF extraction will be affected. Therefore, the range improvement of the LCT-based IF extraction can be studied in the further work.

REFERENCES

[1] Y. Liu et al., "High-resolution real-time imaging processing for spaceborne spotlight SAR with curved orbit via subaperture coherent superposition in image domain," *IEEE J. Sel. Topics Appl. Earth Observ. Remote Sens.*, vol. 15, pp. 1992–2003, Feb. 2022.

[2] J. Deng, H. Bi, J. Zhang, Z. Liu, and L. Yu, "Amplitude-phase CNN-based SAR target classification via complex-valued sparse image," *IEEE J. Sel. Topics Appl. Earth Observ. Remote Sens.*, vol. 15, pp. 5214–5221, Jun. 2022.

[3] P. Huang et al., "Imaging and relocation for extended ground moving targets in multichannel SAR-GMTI systems," *IEEE Trans. Geosci. Remote Sens.*, vol. 60, Aug. 2021, Art. no. 5214024.

[4] R. Cao, Y. Wang, B. Zhao, and X. Lu, "Ship target imaging in airborne SAR system based on automatic image segmentation and ISAR technique," *IEEE J. Sel. Topics Appl. Earth Observ. Remote Sens.*, vol. 14, pp. 1985–2000, Jan. 2021.

[5] Y. Song, J. Zhang, J. Jin, G. Li, and H. Bi, "Frequency scaling based spaceborne squint SAR sparse imaging," *IEEE J. Sel. Topics Appl. Earth Observ. Remote Sens.*, vol. 15, pp. 8064–8073, Sep. 2022.

[6] J. Ding, M. Kahl, O. Loffeld, and P. H. Bolívar, "THz 3-D image formation using SAR techniques: Simulation, processing and experimental results," *IEEE Trans. Terahertz Sci. Technol.*, vol. 3, no. 5, pp. 606–616, Sep. 2013.

[7] C. Deng et al., "Investigation on the motion compensation of the THz SAR," in *Proc. IET Int. Radar Conf.*, 2015, pp. 1–4.

[8] R. Appleby and H. B. Wallace, "Standoff detection of weapons and contraband in the 100 GHz to 1 THz region," *IEEE Trans. Antennas Propag.*, vol. 55, no. 11, pp. 2944–2956, Nov. 2007.

[9] H. Gao et al., "Study of the extended phase shift migration for three-dimensional MIMO-SAR imaging in terahertz band," *IEEE Access*, vol. 8, pp. 24773–24783, 2020.

[10] L. Ding, Y. Ye, G. Ye, X. Wang, and Y. Zhu, "Bistatic synthetic aperture radar with undersampling for terahertz 2-D near-field imaging," *IEEE Trans. Terahertz Sci. Technol.*, vol. 8, no. 2, pp. 174–182, Mar. 2018.

[11] J. Sun, Z. Hao, Q. Li, and D. Li, "Vibration compensation of airborne terahertz SAR based on along track interferometry," *IEEE Geosci. Remote. Sens. Lett.*, vol. 19, Oct. 2021, Art. no. 4019105.

[12] Z. Huang, Z. He, Z. Sun, and Z. Dong, "Ananlysis and compensation of vibration error of high frequency synthetic aperture radar," in *Proc. IEEE Int. Geosci. Remote Sens. Symp.*, 2016, pp. 1138–1141.

[13] H. Xia, Q. Chen, Y. Li, C. Fu, and H. Wang, "A high frequency vibration compensation approach in terahertz SAR based on wavelet multi-resolution analysis," in *Proc. China Int. SAR Symp.*, 2018, pp. 1–5.

[14] W. Xia and L. Huang, "Target vibration estimation in SAR based on phase-analysis method," *EURASIP J. Adv. Signal Process.*, vol. 2016, Sep. 2016, Art. no. 94.

[15] Y. Li, L. Ding, Q. Zheng, Y. Zhu, and J. Sheng, "A novel high-frequency vibration error estimation and compensation algorithm for THz-SAR imaging based on local FrFT," *Sensors*, vol. 20, no. 9, May 2020, Art. no. 2669.

[16] Y. Wang, Z. Wang, B. Zhao, and L. Xu, "Compensation for high-frequency vibration of platform in SAR imaging based on adaptive chirplet decomposition," *IEEE Geosci. Remote Sens. Lett.*, vol. 13, no. 6, pp. 792–795, Jun. 2016.

[17] Y. Li, Q. Wu, J. Wu, P. Li, Q. Zheng, and L. Ding, "Estimation of high-frequency vibration parameters for terahertz SAR imaging based on FrFT with combination of QML and RANSAC," *IEEE Access*, vol. 9, pp. 5485–5496, 2021.

[18] Q. Wang et al., "Reduction of vibration-induced artifacts in synthetic aperture radar imagery," *IEEE Trans. Geosci. Remote Sens.*, vol. 52, no. 6, pp. 3063–3073, Jun. 2014.

[19] Q. Wang et al., "SAR-based vibration estimation using the discrete fractional Fourier transform," *IEEE Trans. Geosci. Remote Sens.*, vol. 50, no. 10, pp. 4145–4156, Oct. 2012.

[20] Y. Wang, Z. Wang, B. Zhao, and L. Xu, "Enhancement of Azimuth focus performance in high-resolution SAR imaging based on the compensation for sensors platform vibration," *IEEE Sens. J.*, vol. 16, no. 16, pp. 6333–6345, Aug. 2016.

[21] S. Shi, C. Li, J. Hu, X. Zhang, and G. Fang, "Study of phase error reconstruction and motion compensation for terahertz SAR with sparsity-promoting parameter estimation," *IEEE Trans. Terahertz Sci. Technol.*, vol. 11, no. 2, pp. 122–134, Mar. 2021.

[22] S. Shi, C. Li, J. Hu, X. Zhang, and G. Fang, "Motion compensation for terahertz synthetic aperture radar based on subaperture decomposition and minimum entropy theorem," *IEEE Sens. J.*, vol. 20, no. 24, pp. 14940–14949, Dec. 2020.

[23] W. Huan, Z. Yuan, B. Wang, and J. Sun, "A novel helicopter-borne terahertz SAR imaging algorithm based on Keystone transform," in *Proc. Int. Conf. Signal Process.*, 2014, pp. 1958–1962.

[24] Y. Zhang, J. Sun, P. Lei, and W. Hong, "SAR-based paired echo focusing and suppression of vibrating targets," *IEEE Trans. Geosci. Remote Sens.*, vol. 52, no. 12, pp. 7593–7605, Dec. 2014.

[25] G. Li and P. K. Varshney, "Micro-Doppler parameter estimation via parametric sparse representation and pruned orthogonal matching pursuit," *IEEE J. Sel. Topics Appl. Earth Observ. Remote Sens.*, vol. 7, no. 12, pp. 4937–4948, Dec. 2014.

[26] B. Peng, X. Wei, B. Deng, H. Chen, Z. Liu, and X. Li, "A sinusoidal frequency modulation Fourier transform for radar-based vehicle vibration estimation," *IEEE Trans. Instrum. Meas.*, vol. 63, no. 9, pp. 2188–2199, Sep. 2014.

[27] S. Shi, C. Li, J. Hu, X. Zhang, and G. Fang, "A high frequency vibration compensation approach for terahertz SAR based on sinusoidal frequency modulation Fourier transform," *IEEE Sens. J.*, vol. 21, no. 9, pp. 10796–10803, May 2021.

[28] Y. Zhao et al., "Vibration error analysis and motion compensation of video synthetic aperture radar," *J. Radars*, vol. 4, no. 2, pp. 230–239, 2015.

[29] X. Zhang, Y. Zhang, and J. Sun, "Effects analysis of helicopter platform vibration on terahertz SAR imaging," *J. Terahertz Sci. Electron. Inf. Technol.*, vol. 16, no. 2, pp. 205–211, 2018.

[30] Z. Wang, Y. Wang, and L. Xu, "Parameter estimation of hybrid linear frequency modulation-sinusoidal frequency modulation signal," *IEEE Signal Process. Lett.*, vol. 24, no. 8, pp. 1238–1241, Aug. 2017.

[31] Y. Guan and Z. Feng, "Adaptive linear chirplet transform for analyzing signals with crossing frequency trajectories," *IEEE Trans. Ind. Electron.*, vol. 69, no. 8, pp. 8396–8410, Aug. 2022.

[32] N. E. Huang et al., "The empirical mode decomposition and the Hilbert spectrum for nonlinear and non-stationary time series analysis," *Proc. Roy. Soc. London A, Math. Phys. Sci.*, vol. 454, no. 1971, pp. 903–995, Mar. 1998.

[33] F. Wu et al., "A 220 GHz terahertz synthetic aperture radar," *J. Terahertz Sci. Electron. Inf. Technol.*, vol. 15, no. 3, pp. 368–371, 2017.

Yong Wang (Senior Member, IEEE) was born in 1979. He received the B.S. and M.S. degrees in electronic engineering and the Ph.D. degree in information and communication engineering from the Harbin Institute of Technology (HIT), Harbin, China, in 2002, 2004, and 2008, respectively.

He is currently a Professor with the Institute of Electronic Engineering Technology, HIT. His main research interests include time–frequency analysis of nonstationary signal, radar signal processing, and their application in synthetic aperture radar imaging.

Dr. Yong Wang has authored or coauthored more than 130 papers, most of them appeared in the journals of IEEE TRANSACTIONS ON GRS, *IET Signal Processing*, *Signal Processing*, etc. He was the recipient of the Program for New Century Excellent Talents in University of Ministry of Education of China in 2012 and the Excellent Doctor's Degree nomination Award in China in 2010.

Siyu Chen was born in 1999. She received the B.S. degree in electronic information engineering from Harbin Institute of Technology (HIT), Harbin, China, in 2021. She is currently working toward the Ph.D. degree in information and communication engineering with HIT.

Her current research interests are in the fields of signal processing and SAR imaging.

Yun Zhang (Member, IEEE) was born in Heilongjiang, China, in November 1975. She received the B.S. and M.S. degrees in electronic engineering and the Ph.D. degree in information and communication engineering from the Harbin Institute of Technology (HIT), Harbin, China, in 2000, 2003, and 2009, respectively.

She is currently a Professor with the Research Institute of Electronic Engineering Technology, HIT. Her research interests include radar signal processing, synthetic aperture radar imaging, machine learning, and pattern analysis in remote sensing.